Cell

Article

TFPI is a colonic crypt receptor for TcdB from hypervirulent clade 2 *C. difficile*

Graphical abstract

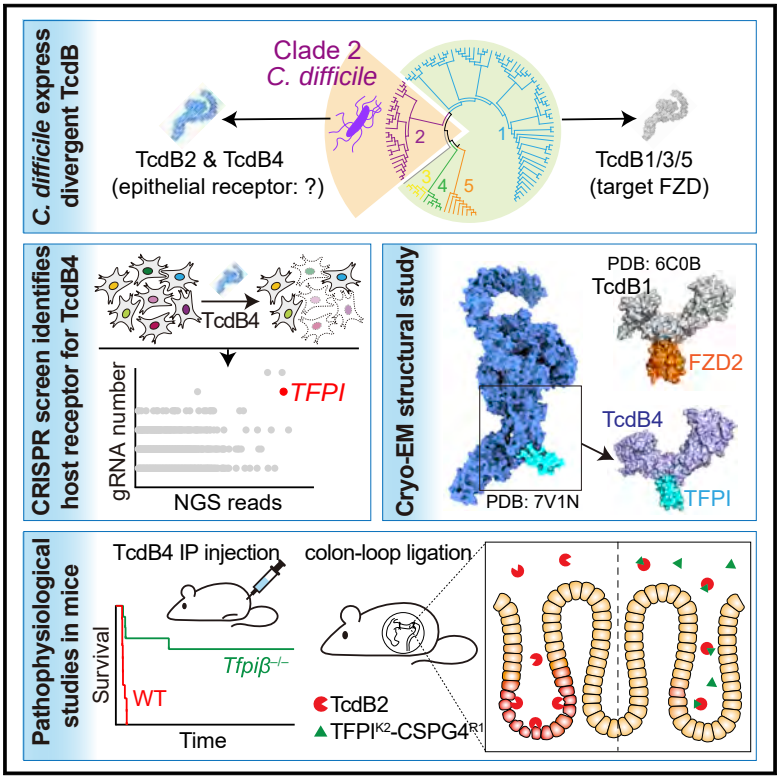

Highlights

- CRISPR screen identifies TFPI as a receptor for TcdB from the clade 2 *C. difficile*
- Cryo-EM structure of TcdB4-TFPI reveals detailed receptor-binding interface
- TFPI is a pathophysiologically relevant receptor for clade 2 *C. difficile* TcdB
- Dual inhibition of TFPI and CSPG4 reduces colonic pathology caused by TcdB2

Authors

Jianhua Luo, Qi Yang, Xiaofeng Zhang, ..., Jing Huang, Yanyan Li, Liang Tao

Correspondence

liyanyan@westlake.edu.cn (Y.L.), taoliang@westlake.edu.cn (L.T.)

In brief

Clade 2 hypervirulent strains of *Clostridioides difficile* express disease-causing toxins TcdB2 and TcdB4, but the intestinal epithelial receptors that allow them to initiate damage have not been known. Here, tissue factor pathway inhibitor (TFPI) was found to be a receptor for both TcdB2 and −4, the TFPI-TcdB4 interaction was structurally characterized, and the ability of TFPI blockers to protect mice from hypervirulent *C. difficile* TcdB-induced intestinal damage was examined.

Luo et al., 2022, Cell *185*, 980–994
March 17, 2022 © 2022 Elsevier Inc.
https://doi.org/10.1016/j.cell.2022.02.010

CellPress

CellPress

Cell

Article

TFPI is a colonic crypt receptor for TcdB from hypervirulent clade 2 *C. difficile*

Jianhua Luo,[1,2,3,8] Qi Yang,[1,2,3,8] Xiaofeng Zhang,[1,2,4,8] Yuanyuan Zhang,[1,2,3,5,8] Li Wan,[1,2,4,8] Xiechao Zhan,[1,2,4] Yao Zhou,[1,2,3] Liuqing He,[1,2,3] Danyang Li,[1,2,3] Dazhi Jin,[6,7] Ying Zhen,[1,2,4] Jing Huang,[1,2,4] Yanyan Li,[1,2,4,*] and Liang Tao[1,2,3,9,*]

[1]Key Laboratory of Structural Biology of Zhejiang Province, School of Life Sciences, Westlake University, Hangzhou, Zhejiang 310024, China
[2]Center for Infectious Disease Research, Westlake Laboratory of Life Sciences and Biomedicine, Hangzhou, Zhejiang 310024, China
[3]Institute of Basic Medical Sciences, Westlake Institute for Advanced Study, Hangzhou, Zhejiang 310024, China
[4]Institute of Biology, Westlake Institute for Advanced Study, Hangzhou, Zhejiang 310024, China
[5]School of Food Science and Biotechnology Engineering, Zhejiang Gongshang University, Hangzhou, Zhejiang 310018, China
[6]Center of Laboratory Medicine, Zhejiang Provincial People's Hospital, People's Hospital of Hangzhou Medical College, Hangzhou, Zhejiang 310014, China
[7]School of Laboratory Medicine, Hangzhou Medical College, Hangzhou, Zhejiang 310014, China
[8]These authors contributed equally
[9]Lead contact
*Correspondence: liyanyan@westlake.edu.cn (Y.L.), taoliang@westlake.edu.cn (L.T.)
https://doi.org/10.1016/j.cell.2022.02.010

SUMMARY

The emergence of hypervirulent clade 2 *Clostridioides difficile* is associated with severe symptoms and accounts for >20% of global infections. TcdB is a dominant virulence factor of *C. difficile*, and clade 2 strains exclusively express two TcdB variants (TcdB2 and TcdB4) that use unknown receptors distinct from the classic TcdB. Here, we performed CRISPR/Cas9 screens for TcdB4 and identified tissue factor pathway inhibitor (TFPI) as its receptor. Using cryo-EM, we determined a complex structure of the full-length TcdB4 with TFPI, defining a common receptor-binding region for TcdB. Residue variations within this region divide major TcdB variants into 2 classes: one recognizes Frizzled (FZD), and the other recognizes TFPI. TFPI is highly expressed in the intestinal glands, and recombinant TFPI protects the colonic epithelium from TcdB2/4. These findings establish TFPI as a colonic crypt receptor for TcdB from clade 2 *C. difficile* and reveal new mechanisms for CDI pathogenesis.

INTRODUCTION

Clostridioides difficile infection (CDI) is a leading cause of nosocomial and community-acquired diarrhea and gastroenteritis-associated death in developed countries, accounting for around half a million cases and 15,000 deaths annually in the United States (Guh et al., 2020; Lessa et al., 2015). In recent years, the global burden of CDI has been exacerbated due to the emergence and widespread of hypervirulent strains (Guh et al., 2020; He et al., 2013; Hunt and Ballard, 2013). The pathogenic *C. difficile* produces 3 pathogenicity-related exotoxins: toxin A (TcdA), toxin B (TcdB), and *C. difficile* transferase (CDT) (Cowardin et al., 2016; Kuehne et al., 2010, 2014). *C. difficile* exploits these toxins to disrupt the intestinal epithelial barrier, cause tissue damage and gain nutrients, provoke or suppress inflammation, and contribute to colonization (Aktories et al., 2017; Cowardin et al., 2016; Fletcher et al., 2021; Pruss and Sonnenburg, 2021; VanInsberghe et al., 2020; Xu et al., 2014). Among the 3 toxins, TcdB plays a key role in causing gastrointestinal diseases, since all pathogenic *C. difficile* contain functional *tcdB* genes, and lacking TcdB, but not TcdA or CDT, could drastically attenuate the virulence of clinical strains in animal models (Carter et al., 2015; Lyras et al., 2009).

TcdB is a member of the large clostridial toxin (LCT) family, which enters target cells via receptor-mediated endocytosis and glucosylates small guanosine triphosphatase (GTPase) proteins, leading to cytoskeletal dysfunction and eventual cell death (Aktories et al., 2017; Chandrasekaran and Lacy, 2017; Voth and Ballard, 2005). Recent genomic and functional studies reported that TcdB can be classified into at least 8 natural variants/subtypes, with type 1 to 4 as major variants associated with human diseases (Shen et al.'s classification is followed hereafter) (Mansfield et al., 2020; Shen et al., 2020). In the colon, the prototypical (type 1; TcdB1) and type-3 TcdB (TcdB3) exploit Wnt receptor Frizzled proteins (FZDs) to disrupt the epithelial barrier and chondroitin sulfate proteoglycan 4 (CSPG4) to impair the intestinal subepithelial

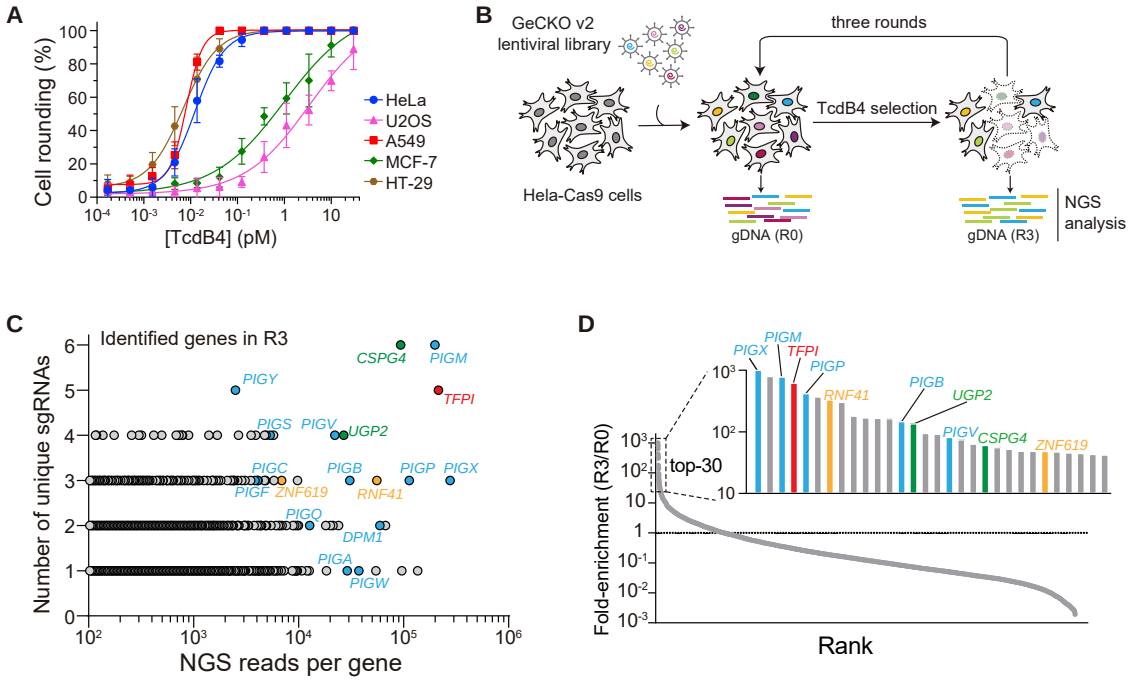

Figure 1. CRISPR-Cas9 screen identifies host factors for TcdB4

(A) The sensitivities of some human cell lines to TcdB4 as measured by cell-rounding assays. Data are presented as mean ± standard deviation (SD) (n = 6).

(B) Schematic diagram of the screening process using TcdB4 on HeLa cells transduced with GeCKO v2 lentiviral library.

(C) Genes identified from the third round of the screen (R3) are ranked and plotted. The x axis shows the number of NGS reads per gene, and the y axis represents the number of unique gRNAs for each targeted gene.

(D) Genes identified are ranked and plotted based on fold enrichment of their gRNA reads from the beginning (R0) to three rounds post-toxin selection (R3). Top 30 enriched genes with at least three gRNAs targeted are marked.

myofibroblasts layer afterward (Chen et al., 2021; Tao et al., 2016). *C. difficile* strains from multi-locus sequence typing (MLST) clade 2, also known as the hypervirulent clade (Stabler et al., 2006), exclusively express two TcdB variants (TcdB2 and TcdB4) that do not recognize FZDs (Chung et al., 2018; Henkel et al., 2020; López-Ureña et al., 2019; Pan et al., 2021). How these TcdB variants target the intestinal epithelium to initiate the damage remains unknown.

Here, we carried out genome-wide CRISPR-Cas9 screens for TcdB4 and identified TFPI as a host receptor. To further understand the molecular basis of TcdB receptor specificity, we determined the structure of the full-length TcdB4 in complex with its receptor TFPI using cryoelectron microscopy (cryo-EM). Based on the structural and phylogenic analysis, we determined that TcdB harbors a key receptor-binding region interacting with either TFPI or FZDs. We further validated that TcdB2, which is produced by several notorious strains including ST01/RT027, also recognizes TFPI. TFPI-mediated intoxication accounts for cryptic damage and epithelial disruption in the intestines and may also be responsible for acute kidney injuries during the systematic infection. Finally, we demonstrated that simultaneously blocking both TFPI- and CSPG4-binding sites is an optimal strategy for neutralizing the clade 2 *C. difficile* TcdB and thus could be developed to prevent and treat CDI caused by the clade 2 *C. difficile*.

RESULTS

CRISPR-Cas9 screen identifies host factors for TcdB4

We set out to perform the gold-standard cytopathic cell-rounding assays on HeLa-Cas9 cells (parental cells; referred to as "wild type" [WT] hereafter) and *CSPG4*$^{-/-}$/*FZD1/2/7*$^{-/-}$ cells to monitor the activities of reference TcdB from each of 8 known subtypes (toxin concentration that induces 50% of cell rounding is defined as CR_{50}). We observed that TcdB4 (reference sequence from strain 8864) is a toxin variant potent to both HeLa WT (CR_{50}: 0.024 pM) and *CSPG4*$^{-/-}$/*FZD1/2/7*$^{-/-}$ cells (CR_{50}: 0.14 pM) (Figure S1). We then tested the sensitivities of some human cell lines to TcdB4. Some cell lines, including U2OS and MCF-7, are much less sensitive to TcdB4 than others, such as HeLa, A549, and HT-29 (Figure 1A). These findings indicate that an uncharacterized and cell type-specific receptor mediates the cellular entry of TcdB4.

To identify the receptor for TcdB4, we conducted a genome-wide CRISPR-Cas9 screen in HeLa cells. In brief, cells were transduced with the GeCKO v2 guide RNA (gRNA) library (Sanjana et al., 2014) using lentiviruses and subjected to 3 rounds of TcdB4 selection (Figure 1B). The gRNAs sequences from the surviving cell population were decoded by next-generation sequencing (NGS). Identified genes were assessed based on fold enrichment of gRNA reads, NGS reads per gene, and the number of unique gRNAs (Figures 1C and 1D).

We focused on the top 30 enriched genes with at least 3 unique gRNAs targeted. *UGP2* and *CSPG4* are 2 expected hits. UGP2 is a cytosolic enzyme that produces uridine diphosphate (UDP)-glucose (Flores-Díaz et al., 1997), a cofactor required for most LCTs to glucosylate small GTPases (Chaves-Olarte et al., 1996; Jank and Aktories, 2008). This gene frequently appeared as a top hit in the previous CRISPR-Cas9 screens for LCTs including TcdA, TcdB, and TcsL (Lee et al., 2020; Tao et al., 2016, 2019), but not Tcnα (Zhou et al., 2021), which uses UDP-N-acetylglucosamine for glucosylation (Selzer et al., 1996). CSPG4 is a characterized receptor for TcdB1 and TcdB2 (Chen et al., 2021; Yuan et al., 2015), and CSPG4 knockout (KO) cells were also mildly resistant to TcdB4 (Pan et al., 2021).

TFPI ranked fourth by fold enrichment and was targeted by 5 different gRNAs. TFPI regulates the tissue factor-dependent pathway of blood coagulation and mainly exists on the cell membrane and in the extracellular space (Broze and Girard, 2012; Wood et al., 2014). Five genes, including *PIGX*, *PIGM*, *PIGP*, *PIGB*, and *PIGV*, encode key proteins in the glycosylphosphatidylinositol (GPI) anchor biosynthesis pathway.

Validation of receptor candidates

To validate the candidates, we generated *TFPI*$^{-/-}$, *PIGX*$^{-/-}$, *PIGM*$^{-/-}$, and *PIGP*$^{-/-}$ HeLa cells using the CRISPR-Cas9 approach. For each candidate gene, 2 single-KO clones were established, and targeted disruptions of the open reading frames were confirmed by DNA sequencing. These cell lines, together with the *FZD1/2/7*$^{-/-}$ and *CSPG4*$^{-/-}$cells, were tested by the cytopathic cell rounding experiment using TcdB4 (Figure 2A).

HeLa *FZD1/2/7*$^{-/-}$ cells remained as sensitive as the WT cells to TcdB4, while *CSPG4*$^{-/-}$ cells showed ~7-fold increased resistance (based on CR_{50} thereafter). HeLa *PIGX*$^{-/-}$, *PIGM*$^{-/-}$, and *PIGP*$^{-/-}$ cells showed modestly reduced sensitivities (~7 to 20 fold) compared with the WT cells to TcdB4 (Figure 2B). GPI anchoring is a posttranslational modification and allows the modified proteins to be attached to the cell membrane via the glycolipid structure. Pretreatment of phosphatidylinositol-specific phospholipase C (PI-PLC), an enzyme that cleaves PI and releases GPI-anchored proteins from the cell membrane, alleviated the cytopathic effect induced by TcdB4 in HeLa cells (Figures 2C and S2A). These results indicate that GPI-anchored protein(s) are involved in TcdB4-induced toxicity to the host cells.

HeLa *TFPI*$^{-/-}$ cells are remarkably resistant to TcdB4, with reduced sensitivity of ~260 fold compared with the WT cells (Figure 2B). The increased resistance in *TFPI*$^{-/-}$ cells was further confirmed by immunoblot for RAC1 glucosylation (Figure 2D). Moreover, we monitored the surface binding of TcdB4 in the HeLa WT, *FZD1/2/7*$^{-/-}$, *CSPG4*$^{-/-}$, and *TFPI*$^{-/-}$cells using the immunoblot assay. TcdB4 is equally bound to the cell surface of WT and *FZD1/2/7*$^{-/-}$ cells. The binding of TcdB4 was slightly reduced in the *CSPG4*$^{-/-}$ cells and drastically diminished in the *TFPI*$^{-/-}$ cells (Figure 2E). These results suggest that TFPI contributes to the toxin action of TcdB4 via mediating the cell surface binding of the toxin.

Membrane-attached TFPI isoforms act as receptors for TcdB4

TFPI has multiple spliced isoforms, since its pre-mRNA undergoes alternative splicing events (Broze and Girard, 2012; Maroney et al., 2010). In humans, TFPI has 2 major isoforms, TFPIα and TFPIβ, which are also produced by all mammals (Wood et al., 2014). TFPIα contains 3 tandem Kunitz-type protease inhibitory (Kunitz-1, Kunitz-2, and Kunitz-3 [or K1, K2, and K3]) domains followed by a basic carboxyterminal (C-terminal) region. TFPIβ lacks the K3 and basic C-terminal domains of TFPIα. Instead, it contains a C-terminal signal peptide that directs cleavage and attachment of a GPI anchor (Broze and Girard, 2012; Girard et al., 2012; Maroney and Mast, 2015; Zhang et al., 2003) (Figure 2F).

TFPIβ is a GPI-anchored protein, which is in line with multiple screen hits in the GPI anchor biosynthesis. Because TcdB4 also binds CSPG4 (yet inefficiently) and CSPG4 is highly expressed in HeLa (Gupta et al., 2017; Tao et al., 2016), we used HeLa *CSPG4*$^{-/-}$ cells to minimize the affection of CSPG4 when studying the roles of TFPI in HeLa. We found that *CSPG4*$^{-/-}$/*TFPI*$^{-/-}$ cells were more resistant to TcdB4 than *CSPG4*$^{-/-}$ cells, while the susceptibility of *CSPG4*$^{-/-}$/*TFPI*$^{-/-}$ cells could be restored by transient transfection of TFPIβ (Figures 2G and 2H).

TFPIα is a secreted isoform that localizes both on the cell surface or in blood plasma (Novotny et al., 1989; Piro and Broze, 2005; Wood et al., 2014). The cell membrane localization of TFPIα is mainly compassed by binding of its K3 domain to protein S and basic C-terminal region to cell-surface glycosaminoglycans (Donahue et al., 2006; Ndonwi et al., 2010, 2012; Piro and Broze, 2004; Sandset et al., 1988). GFP-fused TFPIα, but not $TFPI^{K1+K2}$ (residues 29 to 209), robustly bound to the surface of *CSPG4*$^{-/-}$/*TFPI*$^{-/-}$ cells when supplemented into the culture medium (Figure S2B). We showed that transient transfection of TFPIα restored the susceptibility of *CSPG4*$^{-/-}$/*TFPI*$^{-/-}$cells to TcdB4 (Figures 2G and 2H), indicating TFPIα could also mediate the entry of TcdB4. Consistently, immunoblot analysis showed that overexpression of either TFPIα or TFPIβ mediated robust binding of TcdB4 on the cell surface (Figure 2I). Collectively, these data demonstrate that membrane-attached TFPI, in both α and β isoforms, serve as cellular receptors for TcdB4.

Interestingly, we found that "free" TFPIα has binary effects on mediating the cellular entry of TcdB4, depending on the presence of cell surface TFPI. Cultured *CSPG4*$^{-/-}$/*TFPI*$^{-/-}$ cells express no TFPI and allow exogenous TFPIα to bind. Thus, we observed that the supplemented TFPIα-GFP bound to the surface of the *CSPG4*$^{-/-}$/*TFPI*$^{-/-}$ cells and mediated the entry of TcdB4 (Figures 2J, S2B, and S2C). In contrast, the cell surface of *CSPG4*$^{-/-}$ cells is expected to be saturated by endogenous-expressed TFPIα. Indeed, TFPIα-GFP protected *CSPG4*$^{-/-}$ cells from TcdB4 in a dose-dependent manner (Figures 2J and S2C).

The K2 domain of TFPI interacts with TcdB4

Because both TFPIα and TFPIβ can mediate the binding/entry of TcdB4, we conjectured that TcdB4 interacts with the K1 and K2 domains of TFPI ($TFPI^{K1+K2}$). Thus, we used recombinant $TFPI^{K1+K2}$ fused with human fragment crystallizable (Fc) region

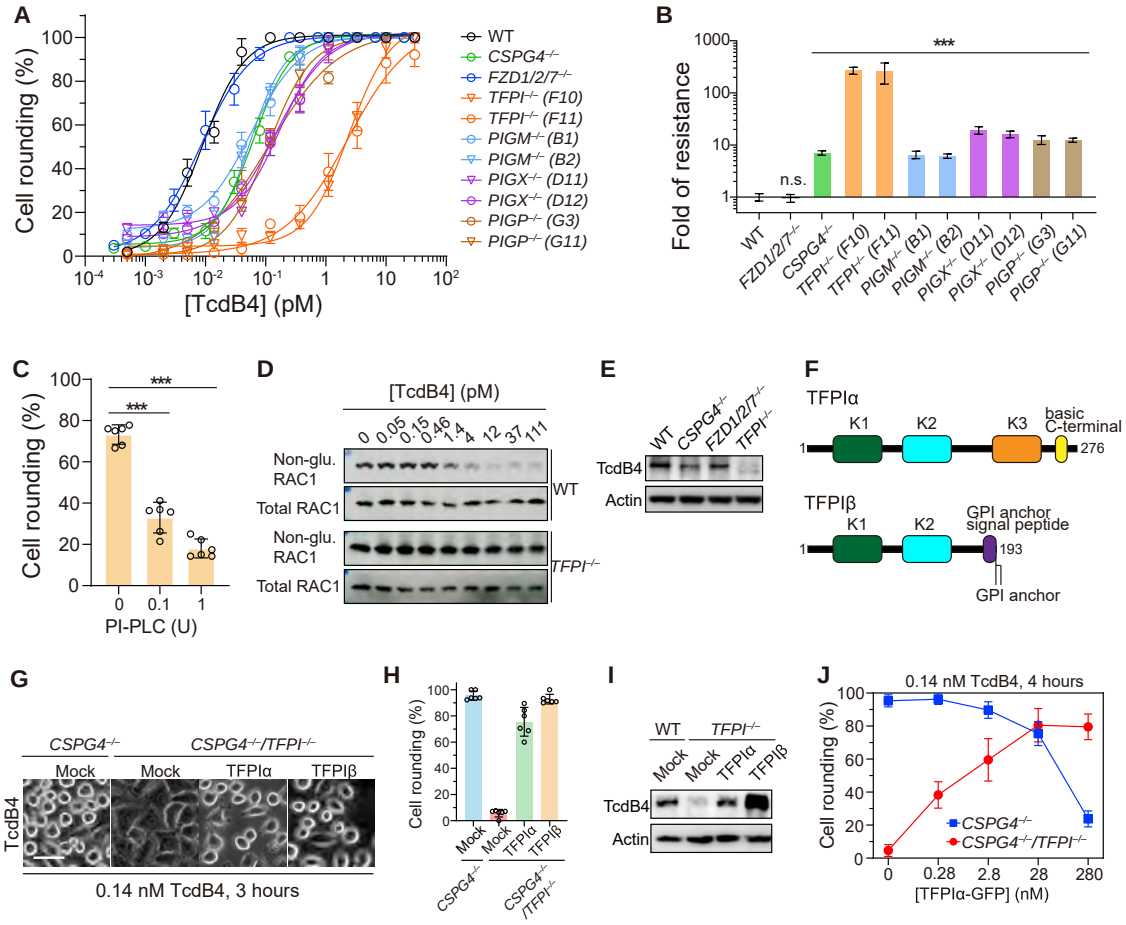

Figure 2. TFPI is a cellular receptor for TcdB4

(A) The sensitivities of the indicated HeLa KO cells to TcdB4 were measured using cell-rounding experiments. Error bars (n = 6) indicate mean ± SD.

(B) The measured sensitivities in (A) are quantified and represented as "fold of resistance" compared to HeLa WT cells. Error bars (n = 6) indicate mean ± SD; ***p < 0.001 versus WT (Student's t test).

(C) WT cells were pretreated with or without PI-PLC and tested for their sensitivities to TcdB4. The percentages of cell rounding at 2.5 h post-TcdB4 exposure are plotted as a bar chart. Data (n = 6) are presented as mean ± SD; ***p < 0.001 (Student's t test).

(D) The sensitivities of HeLa *TFPI*$^{-/-}$ cells versus the WT cells to TcdB4 were compared by analyzing the glucosylation levels of RAC1 using immunoblot assays.

(E) Cell surface-bound TcdB4 in HeLa WT, *CSPG4*$^{-/-}$, *FZD1/2/7*$^{-/-}$, or *TFPI*$^{-/-}$ cells was detected by immunoblot analysis. Actin is a loading control.

(F) Schematic illustrations of TFPIα and TFPIβ.

(G) Transient transfection of TFPIα or TFPIβ restored TcdB4 entry into HeLa *CSPG4*$^{-/-}$/*TFPI*$^{-/-}$ cells (0.14 nM TcdB4; 3 h). Scale bar, 50 μm.

(H) Quantification of the cell rounding in (G). Error bars indicate mean ± SD (n = 6).

(I) Cell surface-bound TcdB4 in HeLa WT or *TFPI*$^{-/-}$ cells transfected with TFPIα, TFPIβ, or mock was detected by immunoblot analysis. Actin is a loading control.

(J) TcdB4 (0.14 nM; 4 h) induced cytopathic effects of *CSPG4*$^{-/-}$ and *CSPG4*$^{-/-}$/*TFPI*$^{-/-}$ cells in the presence or absence of TFPIα-GFP were quantified by the cell-rounding assay. Data are presented as mean ± SD (n = 6).

(Figure 3A) to perform the competition assay on the HeLa *CSPG4*$^{-/-}$ cells. TFPI^{K1+K2} effectively protected the cells from TcdB4 but failed to alleviate the intoxication of TcdB1 (Figures 3B and S3A), indicating TFPI^{K1+K2} specifically binds TcdB4. Also, TcdB4, but not TcdB1, was bound to the recombinant TFPI^{K1+K2}-Fc and co-precipitated by Protein A beads (Figure S3B).

Kunitz domains are small, rich in disulfide, and α/β fold structural domains that function as protease inhibitors (Ascenzi et al., 2003). Kunitz domains can be found in many proteins including TFPI, TFPI2, alpha-1-microglobulin/bikunin precursor (AMBP), and amyloid precursor protein. Phylogenic analysis showed that the primary sequence of TFPI^{K2} is most closely related to TFPI^{K1} with 67.9% sequence similarity, followed by TFPI2^{K1} (64.1% similarity), whereas TFPI^{K3} is less similar to either TFPI^{K1} (56.6% similarity) or TFPI^{K2} (58.5% similarity) (Figure 3C).

To determine whether TcdB4 binds to TFPI^{K1} or TFPI^{K2} and the binding selectivity, we expressed GPI-anchored TFPI^{K1}, TFPI^{K2}, TFPI2^{K1}, or AMBP^{K3} in the HeLa *CSPG4*$^{-/-}$/*TFPI*$^{-/-}$ cells and then tested their sensitivities to TcdB4. Transient transfection of only GPI-anchored TFPI^{K2} could restore the

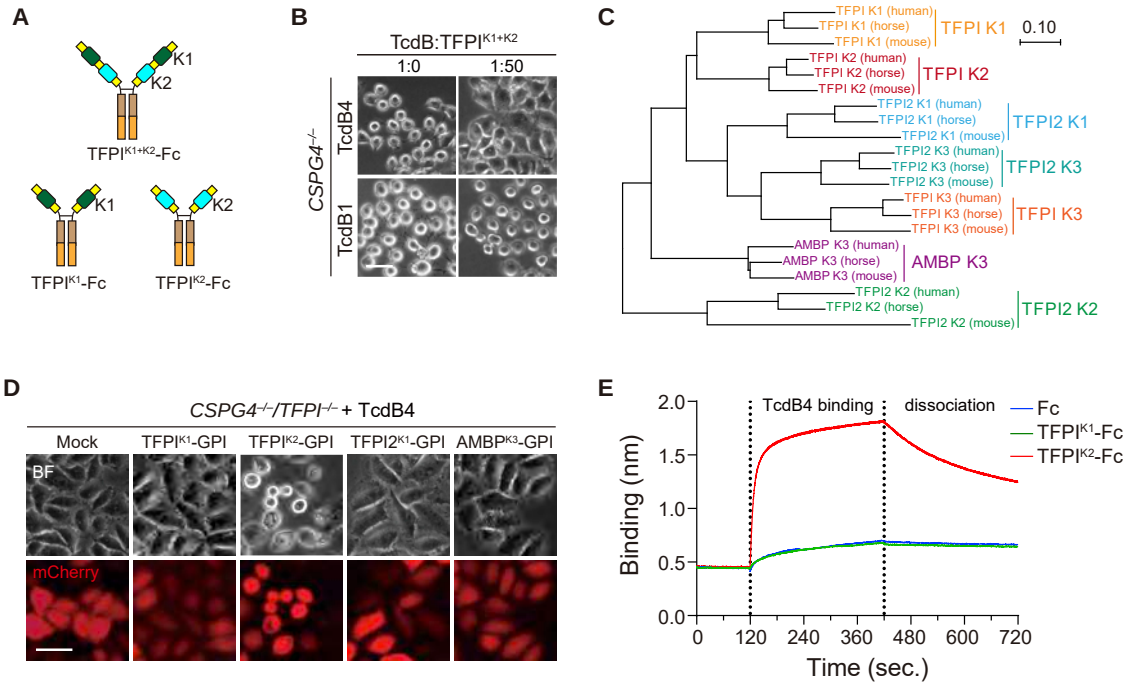

Figure 3. TcdB4 interacts with the Kunitz-2 domain of TFPI

(A) Schematic illustrations of TFPI^{K1+K2}-Fc, TFPI^{K1}-Fc, and TFPI^{K2}-Fc.

(B) TFPI^{K1+K2} protects the HeLa *CSPG4*$^{-/-}$ cells from TcdB4, but not TcdB1.

(C) Phylogenic tree of closely related Kunitz domains from TFPI, TFPI2, and AMBP.

(D) Ectopic expression of GPI-anchored TFPI^{K2} (TFPI^{K2}-GPI) restored TcdB4 entry into *CSPG4*$^{-/-}$/*TFPI*$^{-/-}$ cells.

(E) Characterization of TcdB4 binding to Fc-tagged TFPI^{K1} or TFPI^{K2} using the BLI assay (see Figure S3 for K_d analysis). Human immunoglobin G (IgG) Fc serves as a control.

susceptibility of *CSPG4*$^{-/-}$/*TFPI*$^{-/-}$ cells (Figure 3D), suggesting TcdB4 specifically recognizes TFPI^{K2}. Consistently, TFPI^{K2}-Fc, but not TFPI^{K1}-Fc, protected the HeLa *CSPG4*$^{-/-}$ cells in the competition assay (Figure S3C).

We next quantified the binding kinetics between TFPI^{K1+K2}-Fc and TcdB4 using the bio-layer interferometry (BLI) assay, which revealed a high affinity with a dissociation constant (K_d) of ~13 nM (Figure S3D). BLI assay also showed that TcdB4 bound to TFPI^{K2}-Fc with a K_d of ~6 nM, but not to TFPI^{K1}-Fc or human Fc fragment (Figures 3E and S3E). Similarly, TcdB4 bound to Fc-tagged mouse Tfpi^{K2} with a K_d of ~4 nM (Figure S3F).

Cryo-EM structure of TcdB4-TFPI complex

TcdB (~270 kDa) is one of the largest bacterial toxins composed of 4 domains, including a glucosyltransferase domain (GTD), cysteine protease domain (CPD), transmembrane delivery and receptor-binding domain (DRBD), and C-terminal combined repetitive oligopeptides (CROPs) domain (Figure 4A). To characterize the TcdB4-TFPI interaction, the full-length TcdB4 were mixed with TFPI^{K1+K2}, and the complex was then isolated by size-exclusion chromatography. The complex fractions were confirmed by SDS-PAGE and concentrated for cryo-EM sample preparation (Figures S4A–S4C). The two-dimensional class averages of the TcdB4-TFPI complex showed clear structural features (Figures S4D–S4F). The final maps of the full-length TcdB4 core region resolution at 3.1 Å and the TcdB4-TFPI complex at 3.7 Å resolution under neutral pH conditions reveal most side-chain densities and secondary structural elements (Figures 4B and S4G–S4K).

The overall architecture of TcdB4 is similar to the known structures of TcdB1 (Simeon et al., 2019) and TcdB3 (Chen et al., 2019a). The CPD and GTD form an integrated region while the CROPs domain module curve around the core region by forming like a big hook (Figure 4B). TFPI^{K2} binds to the convex edge of the DRBD (residues 841–1,834) largely through 2 flexible loops in TFPI: loop 1 (residues 131–138) and loop 2 (residues 155–162) (Figures 4B and 4C). Each loop engages TcdB4 via an extensive network composed of hydrogen bonds and hydrophobic interactions (Figure 4D). The interaction between TcdB4^{DRBD} and TFPI^{K2} was further validated by the pulldown assay (Figure S5A). Point mutations at L1599, K1435, L1434, V1492, L1494, M1438, and D1468 in TcdB4 abolish the TFPI-binding ability, suggesting these positions are important for receptor recognition (Figure 4E).

Previous studies showed that the K2 domain of TFPI binds to the trypsin-like substrates such as factor Xa (FXa) (Brandstetter et al., 1996; Burgering et al., 1997). Structurally, TFPI^{K2} interacts with both FXa and TcdB4 through the same loops (Figure S5B).

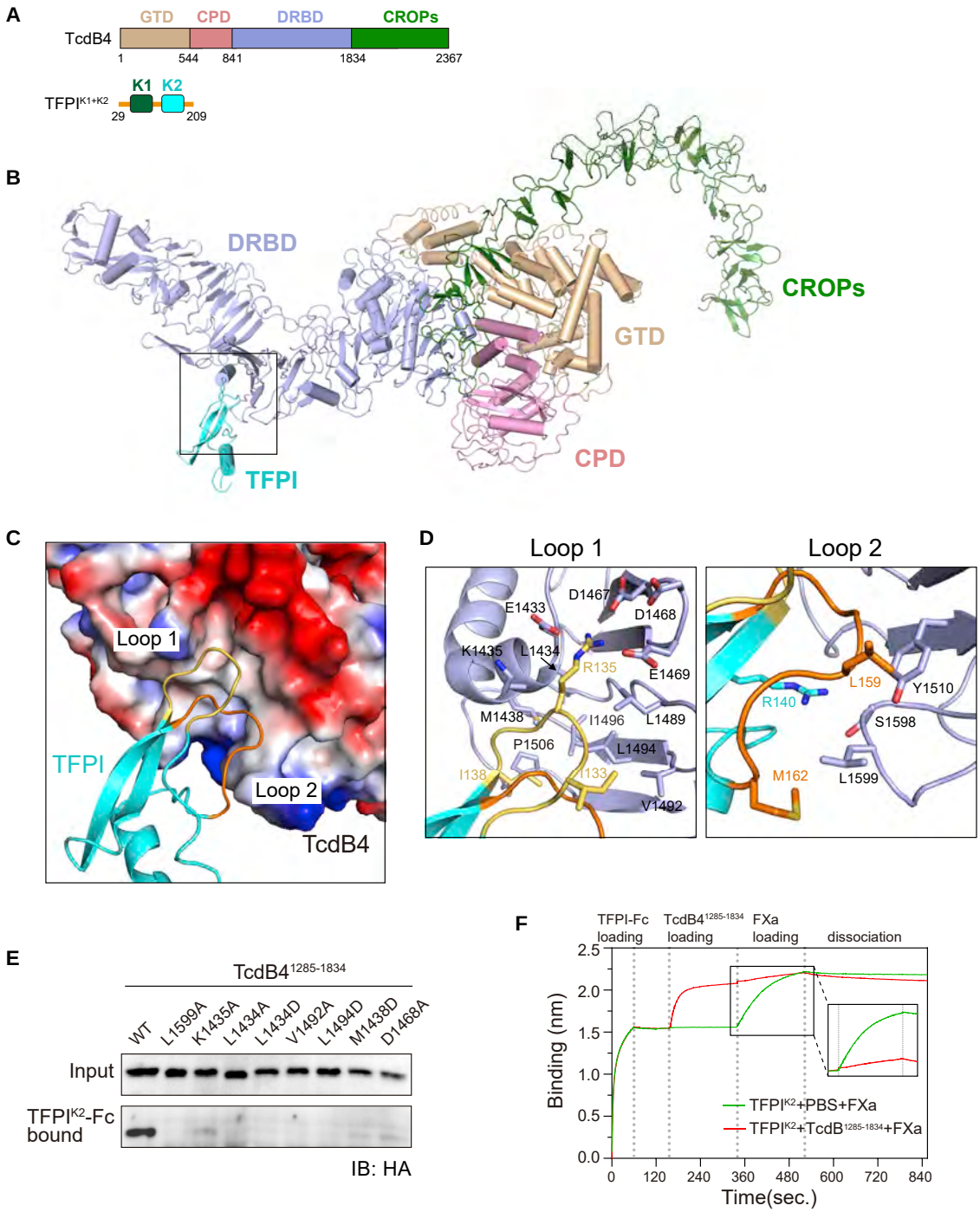

Figure 4. Cryo-EM structure of TcdB4-TFPI complex

(A) Schematic diagrams of the domain organization of full-length TcdB4 and $TFPI^{K1+K2}$ used for cryo-EM structure determination.

(B) Cryo-EM structure of the TcdB4-TFPI complex. The GTD, CPD, DRBD, and CROPs of TcdB4 are shown in wheat, pink, light blue, and green, respectively. $TFPI^{K2}$ is shown in cyan.

(C) Zoomed-in view of the interaction between $TcdB4^{DRBD}$ (electrostatic surface) and $TFPI^{K2}$ (cyan).

(D) Close-up views on the loop1-TcdB4 (left panel) and loop2-TcdB4 (right panel) binding interface.

(E) Mutations in $TcdB4^{1285–1834}$ disrupting its interactions with Fc-tagged $TFPI^{K2}$ were demonstrated by a pulldown assay.

(F) Preloading $TcdB4^{1285–1834}$ to $TFPI^{K2}$ impeded the subsequent binding of FXa. The $TFPI^{K2}$-Fc loaded biosensors were first exposed to 300 nM $TcdB4^{1285–1834}$ or control buffer, balanced, and then exposed to 100 nM FXa.

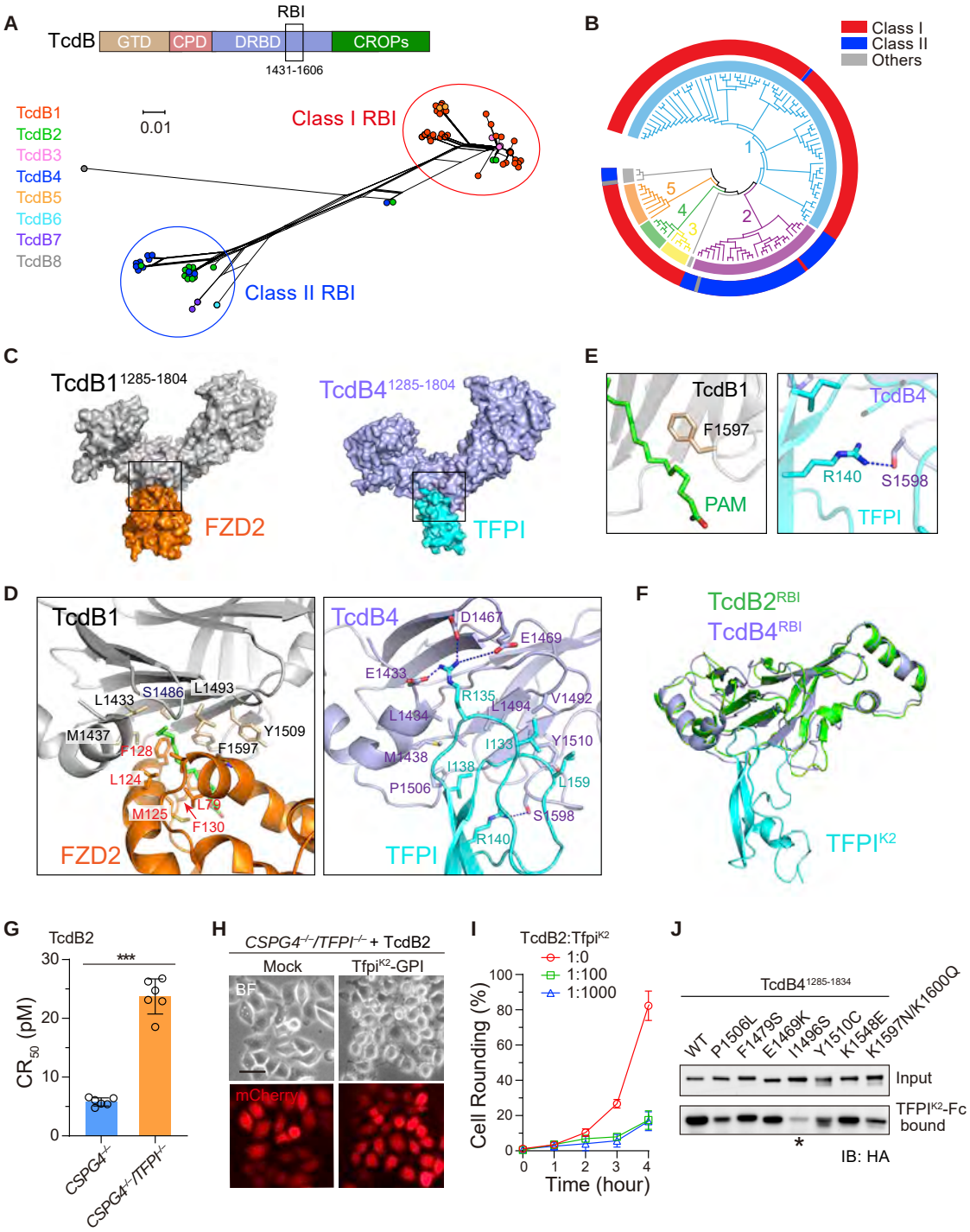

Figure 5. TcdB contains 2 classes of RBIs recognizing either FZDs or TFPI

(A) The schematic illustration of the RBI in TcdB (upper panel) and a phylogenic split network covering RBIs from known TcdB sequences (lower panel).

(B) A maximum-likelihood tree was built for 110 MLST types to separate 5 major *C. difficile* clades (inner ring: clade 1 in light blue, clade 2 in purple, clade 3 in yellow, clade 4 in green, clade 5 in orange, and gray for other cryptic clades). RBI classes in each MLST type are marked as the outer ring.

(C) Structural comparison between the TcdB1-FZD2 complex (PDB:6C0B; left panel) and the TcdB4-TFPI complex (right panel). Only DRBDs (residues 1,285–1,804) of TcdB1 (gray) and TcdB4 (light purple) are shown.

(D) Close-up view on the TcdB1-FZD2 (left panel) and TcdB4-TFPI (right panel) interfaces. Key residues and PAM are shown as stick models.

(E) F1597 in TcdB1 stabilizes the middle part of PAM, while S1598 (corresponding residue) in TcdB4 forms a close hydrogen bond with R140 from TFPI.

(F) Superposition of RBIs from TcdB2 (green; PDB: 6OQ5) and that from TcdB4-TFPI complex (light purple).

(legend continued on next page)

Using the BLI assay, we demonstrated that the prebound of TcdB4$^{1285–1834}$ to TFPI blocked the binding of FXa and vice versa (Figures 4F and S5C).

Determination of receptor-binding specificities of TcdB variants

The resolved structure of TcdB4-TFPI, together with the previously reported structure of TcdB1-FZD2 (Chen et al., 2018), revealed an evolutionarily functional region in TcdB for receptor recognition. To predict the receptor specificities of divergent TcdB sequences, we performed a phylogenetic analysis on the receptor-binding interface (RBI) of TcdB (residues 1,431–1,606) (Figure 5A). The phylogenetic tree is clustered into 2 major branches (denoted as Class I and II). Class I RBIs derive from TcdB1, TcdB3, and TcdB5, which prefer to bind FZDs. Class II RBIs were composed of sequences from TcdB2, TcdB4, TcdB6, and TcdB7 (Figure 5A), mainly existing in clade 2 *C. difficile* (Figure 5B). A small number of RBIs from TcdB2 and TcdB4 were found either in Class I or as outliers, possibly due to the historically frequent recombination events among TcdB variants (Knight et al., 2021; Mansfield et al., 2020; Shen et al., 2020). We also perform the cytopathic cell-rounding assays on the HeLa *CSPG4*$^{-/-}$ and *CSPG4*$^{-/-}$/*TFPI*$^{-/-}$ cells using reference TcdB1–8. Consistent with the phylogenetic analysis result, knocking out TFPI reduced the sensitivity of the cells to TcdB2, TcdB4, TcdB6, and TcdB7 (Figures S6A and S6B).

Albeit FZD2 and TFPI are structurally divergent, they both engage the same hydrophobic interface located on the convex edge of TcdB^{RBI} (Figure 5C). Several residues, including but not limited to L1434, M1438, L1494, and Y1510 (positions in TcdB4; residues in TcdB1 shift to the left by one position in the alignment), are shared by Class I and Class II RBIs and contribute to both FZD and TFPI interactions. In the TcdB1-FZD2 complex, the interaction is bridged by a palmitoleic acid (PAM) with its tail protruding into a hydrophobic pocket in TcdB1. In the TcdB4-TFPI complex, the side chain of TFPI R135 is deeply embedded in the same pocket and forms multiple hydrogen bonds with adjacent residues including E1433, D1467, and E1469 from TcdB4 (Figure 5D). F1597 in TcdB1 is a critical residue stabilizing the middle part of PAM and interacts with the nearby F130 in FZD2 (Chen et al., 2018, 2019b), while the F1597S substitution mimicking TcdB2 (F1598S for TcdB4) abolishes FZD binding (Henkel et al., 2020). Remarkably, S1598 in TcdB4 forms a close hydrogen bond with the nearby R140 in TFPI (Figure 5E). Thus, an F1598S substitution for TcdB may impair FZD binding but contribute to TFPI binding. Accordantly, phenylalanine is conserved in all Class I RBIs while serine is conserved in all Class II RBIs at this position.

The potential TFPI-binding interface in TcdB2 (reference sequence from R20291, an ST01/RT027 strain) resembles TcdB4 (Figure 5F), providing a structural clue that TcdB2 may recognize TFPI. As expected, the HeLa *CSPG4*$^{-/-}$/*TFPI*$^{-/-}$ cells are more resistant to TcdB2 than its parental *CSPG4*$^{-/-}$ cells (Figure 5G), while its susceptibility could be restored by ectopic expressing a GPI-anchored Tfpi^{K2} (Figure 5H). In addition, Tfpi^{K2}-Fc effectively protected the HeLa *CSPG4*$^{-/-}$ cells from TcdB2 intoxication (Figures 5I and S6C). BLI analysis revealed that TcdB2 bound to Fc-tagged mouse Tfpi^{K2} and human TFPI^{K2} with respective K_d of ~0.2 and 0.4 μM (Figures S6D–S6F).

There are a few different residues between TcdB2 and TcdB4 within the RBI (Figure S6G). To interrogate the residues in TcdB2 that cause reduced binding of TFPI, we generated a series of TcdB4$^{1285–1834}$ mutants by replacing the residues with the corresponding ones in TcdB2. The pulldown experiment showed that I1496S is a key mutation attenuating the TFPI binding, while substitutions P1506L, Y1510C, and K1597N/K1600Q slightly reduce the interaction (Figure 5J). On the other hand, an S1496I substitution within TcdB2$^{1285–1834}$ enhanced its binding affinity to both human and mouse TFPI (Figures S6H and S6I).

TFPI is a physiologically relevant receptor for TcdB4

TFPI is primarily produced by endothelial cells, megakaryocytes, monocytes, and smooth muscle cells (Maroney and Mast, 2015; Wood et al., 2014). In human intestines, TFPI is highly expressed in endothelial cells and glandular cells (Uhlén et al., 2015). We also confirmed the Tfpi expression at the base of the glands in mouse intestines, including ileum, jejunum, cecum, and colon, via immunohistochemistry (IHC) analysis (Figures 6A and S7A).

To study the role of TFPI in TcdB4-induced colonic damage, we performed the mouse colon loop ligation experiment, which has been commonly used to examine the tissue damages caused by *C. difficile* toxins (Sun et al., 2010). Saline, TcdB4 (2 μg), or TcdB4 (2 μg) premixed with TFPI^{K2}-Fc (100 μg) were injected into the lumens of ligated colon segments. After six h, mice injected with TcdB4 alone developed obvious intoxication symptoms, including reduced mobility, hunched posture, and eye squinting, while mice injected with saline or TcdB4 premixed with TFPI^{K2}-Fc showed normal activities. By using hematoxylin and eosin (H&E) staining and immunofluorescent labeling for ZO-1, we observed largely collapsed colonic crypts and partly disrupted cryptic epithelium in the TcdB4 group, indicating colonic crypts are vulnerable to TcdB4. As expected, co-injection of TFPI^{K2}-Fc effectively prevented the TcdB4-induced erosion of colonic crypts (Figures 6B–6D and S7B).

To further investigate the role of TFPI *in vivo*, we turned to Tfpi-KO mouse models. Although complete disruption of Tfpi in mice is intrauterine lethal (Huang et al., 1997), mice with

(G) Sensitivity of the HeLa *CSPG4*$^{-/-}$and *CSPG4*$^{-/-}$/*TFPI*$^{-/-}$ cells to TcdB2 were measured using the cell-rounding assay, and their CR_{50} are plotted in a bar chart. (***$p < 0.001$)

(H) Ectopic expression of GPI-anchored Tfpi^{K2} (Tfpi^{K2}-GPI) restored TcdB2 entry into the *CSPG4*$^{-/-}$/*TFPI*$^{-/-}$ cells. Scale bar represents 50 μm.

(I) Protection from TcdB2 using mouse Tfpi^{K2}-Fc on HeLa *CSPG4*$^{-/-}$ cells was quantified by the cell-rounding assay over time. Data are presented as mean ± SD (n = 6).

(J) Point mutations on TcdB4$^{1285–1834}$ were examined in pull-down assays, using TFPI^{K2}-Fc as bait. Bound TcdB4$^{1285–1834}$ mutants were co-precipitated with TFPI^{K2}-Fc using the protein A resin and detected by immunoblot analysis.

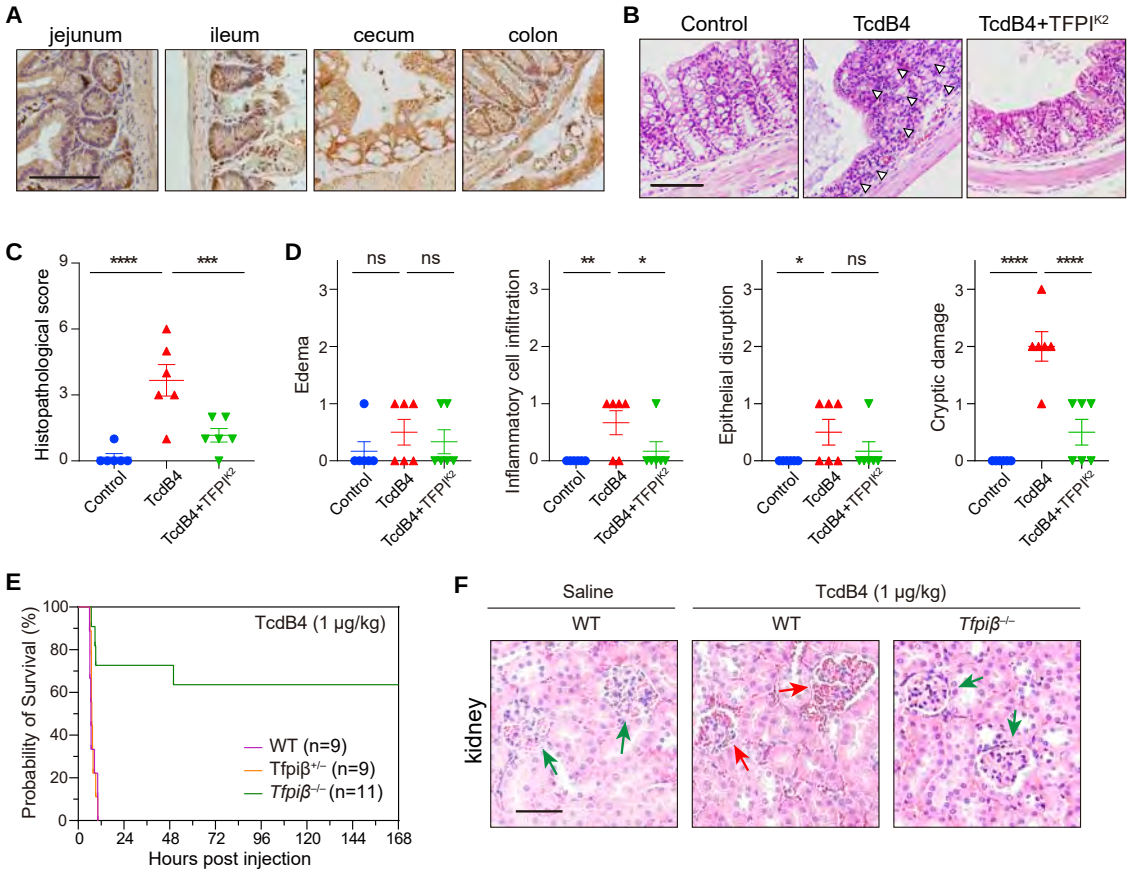

Figure 6. TFPI is a physiologically relevant receptor for TcdB4

(A) Mouse ileum, jejunum, cecum, and colon paraffin sections were subjected to IHC analysis to detect Tfpi. Blue staining indicates cell nuclei, brown staining indicates Tfpi. Scale bar represents 100 μm.

(B) Mouse colonic tissues harvested after colon loop ligation assays were assessed for the histopathology induced by TcdB4 (2 μg) with or without TFPI^{K2}-Fc (50 μg) through H&E staining. Eroded crypts are marked by hollow triangles. Representative images are shown. Scale bar represents 100 μm.

(C and D) Histopathological scores (n = 6 mice) for (B) were assessed based on indicated pathological features (D). Overall scores were summarized in (C). Error bars indicate mean ± standard error of the mean (SEM); one-way ANOVA using Fisher LSD test for multiple comparisons. ****$p < 0.0001$, ***$p < 0.001$, **$p < 0.01$, *$p < 0.05$, ns = not significant.

(E) Survival of the WT, *Tfpiβ*$^{+/-}$, and *Tfpiβ*$^{-/-}$ mice after i.p. injection of 1 μg/kg TcdB4 illustrated by the Kaplan-Meier curves (monitored for 7 days).

(F) Kidney tissues from the WT and *Tfpiβ*$^{-/-}$ mice were harvested after i.p. injection of 1 μg/kg TcdB4 and assessed by H&E staining. Normal (green arrows) and damaged (red arrows) glomerulus were denoted. Scale bar represents 50 μm.

partial Tfpi retained appear to exhibit no overt developmental defect (Girard et al., 2018). Therefore, we generated the Tfpiβ KO mice (more precisely, β+γ isoforms KO) using the CRISPR-Cas9 approach (Figure S7C). When intraperitoneal (i.p.) injected with TcdB4 (1 μg/kg), all tested WT (*Tfpiβ*$^{+/+}$) mice and heterozygous (*Tfpiβ*$^{+/-}$) mice died rapidly within 12 h. Strikingly, 63.6% (7 out of 11) of the homozygous KO (*Tfpiβ*$^{-/-}$) mice survived (Figure 6E), with no obvious gender difference in lethality (Figure S7D). These results demonstrate that Tfpi is a physiological receptor of TcdB4 during systematic toxin exposure. The immunoblot analysis reveals reduced Tfpi levels in the *Tfpiβ*$^{-/-}$ mice, particularly in the kidney, presumably because kidneys mainly expresses the Tfpiβ isoform (Figure S7E). Based on the histopathological analysis, i.p. injecting TcdB4 in the WT mice leads to acute kidney damage, including glomerulus and retrobulbar capillaries dilate, structural damage of red blood cells, hemoglobin deposition of hemoglobin in the intravascular, and renal interstitial congestion and bleeding. Livers, lungs, spleens, and hearts in all injected mice seem to be normal. In comparison, *Tfpiβ*$^{-/-}$ mice injected with TcdB4 showed normal kidneys (Figures 6F and S7F). These data indicate that TcdB4 entering the circulation system, which is common in severe infections, may strongly damage the kidney and cause death.

Simultaneous blocking TFPI and CSPG4 binding offers optimal protection from the clade 2 *C. difficile* TcdB

Besides TcdB4, TcdB2 is the other major variant expressed by clade 2 *C. difficile*. To examine whether impeding TFPI binding also protects the colonic epithelium from TcdB2, we further performed colon loop ligation assays using TcdB2 and TFPI^{K2}-Fc. TcdB2 caused severe intestinal injuries, including edema,

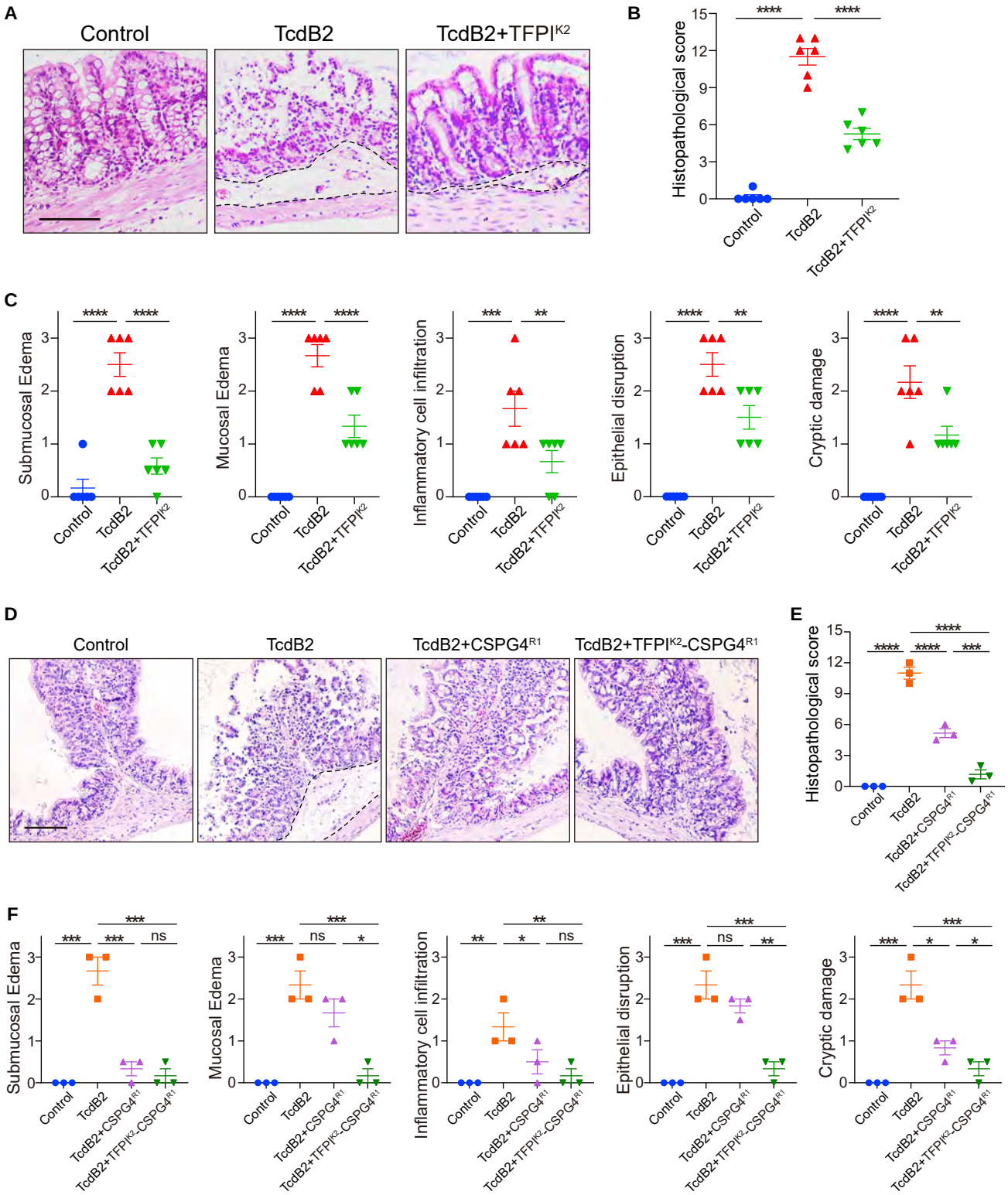

Figure 7. Simultaneous blocking TFPI and CSPG4 binding offers optimal protection from the clade 2 *C. difficile* TcdB

(A) Mouse colonic tissues harvested after colon loop ligation assays were assessed for the histopathology induced by TcdB2 (2 μg) with or without TFPI^{K2}-Fc (50 μg) through H&E staining. Submucosal edema is highlighted by dashed lines. Representative images are shown. Scale bar represents 100 μm.

(B and C) Histopathological scores (n = 6 mice) for (A) were assessed based on indicated pathological features (C). Overall scores were summarized in (B).

(legend continued on next page)

epithelial disruption, and inflammatory cell infiltration, which was in line with the previous studies (Chen et al., 2021; Pan et al., 2021). For mice co-injected with TcdB2 and TFPI^{K2}-Fc, all above pathological features, particularly submucosal edema, were alleviated (Figures 7A–7C). However, this protection still seemed to be suboptimal for TcdB2. Since TcdB2 additionally utilizes CSPG4 as its high-affinity receptor, the residual tissue damage may be due to the CSPG4-mediated toxin entry.

On the other hand, blockage of CSPG4 binding also partly protected the intestinal epithelium from TcdB2, and the previous study used CSPG4$^{410–550}$ (CSPG4^{R1}) as an inhibitor to reduce the TcdB damage in the mouse models (Chen et al., 2021). Based on the structural features of the toxin-receptor binding, it would be feasible to simultaneously block both TFPI- and CSPG4-binding sites on TcdB2. Therefore, we generated a TFPI^{K2}-CSPG4^{R1} fusion construct with a flexible linker (GGGGS × 3) and evaluated its ability to inhibit TcdB2-induced toxicity *in vivo* using the mouse colon loop model. In brief, TcdB2 (2 μg), TcdB2 premixed with CSPG4^{R1} (50 μg), or TcdB2 premixed with TFPI^{K2}-CSPG4^{R1} (50 μg) were injected into the lumens of ligated mouse colon segments, and the colon tissues were then dissected out for histopathological analysis 6 h post-injection. CSPG4^{R1} partly reduced TcdB2-induced damage to the colon, including inflammatory cell infiltration and submucosal edema, which is in line with the previous report. Compared to CSPG4^{R1}, TFPI^{K2}-CSPG4^{R1} provided further enhanced protection to colon tissues albeit an indeed lower toxin-inhibitor molar ratio was adopted, particularly in reducing mucosal edema, epithelial disruption, and cryptic damage (Figures 7D–7F). Together, these results suggest a possible therapeutic avenue of simultaneous inhibiting both TFPI- and CSPG4-binding abilities, which provides optimal protection from the clade 2 *C. difficile* TcdB.

DISCUSSION

Clinical strains belonging to *C. difficile* clade 2 are frequently isolated in North America, Europe, and Australia, accounting for over 20% of global CDI (Badilla-Lobo and Rodríguez, 2021; He et al., 2013; Knight et al., 2021). The clade 2 lineages have been generally concerned not only because they are epidemically associated with severe symptoms but also because they exclusively produce variant forms of TcdB that exhibit varied biological activities including receptor recognition (Lanis et al., 2010; Quesada-Gómez et al., 2016; Stabler et al., 2008). These TcdB variants fail to bind FZDs but retain varied CSPG4-binding abilities (Pan et al., 2021). However, CSPG4 is absent in the intestinal epithelium, as validated in multiple studies (Mileto et al., 2020; Tao et al., 2016; Terada et al., 2006). Here, we showed that TFPI is a functional receptor for TcdB from clade 2 *C. difficile*. More importantly, TFPI is highly expressed in human and mouse intestinal glandular epithelia (Uhlén et al., 2015). Our discovery of TFPI as a physiologically relevant receptor for TcdB4 and TcdB2 fills the gap of how TcdB from clade 2 *C. difficile* targets the colonic epithelium to initiate the tissue damage.

The cryo-EM structure of TcdB4-TFPI revealed an interacting pattern that is similar to TcdB1-FZD2 and TcsL-SEMA6A (Chen et al., 2018; Lee et al., 2020). The finding solidifies the notion that LCTs have evolved to bind different receptors via a similar interacting region. Remarkably, this is the first co-structure of a full-length LCT in complex with its receptor. The structure of the core domains of the toxin resembles the previously reported full-length TcdB structures (Chen et al., 2019a; Simeon et al., 2019). Based on the co-structure, we further deduced that TcdB2, which is expressed by several notorious *C. difficile* genotypes including ST01/RT027, could recognize TFPI as well. The reference sequence of TcdB2 bound mouse Tfpi and human TFPI with the K_d of ~0.2 and ~0.4 μM. The attenuation of the affinity (K_d for TcdB4-TFPI is ~13 nM) is mainly due to a residue change of I1496S in TcdB2, while substitutions at other positions may also be involved. Notably, I1496 is found in certain TcdB2 sequences; those TcdB2 may exhibit strong binding to TFPI.

The discovery that TcdB variants can exploit two types of cellular receptors, TFPI and FZDs, to target the host intestinal barrier largely expands our perception of CDI pathogenesis. TcdB variants are sequentially divergent; the primary sequence identity between TcdB1 and TcdB4 is only 85.6%. Our finding that TcdB1 and TcdB4 adopt different sorts of proteins as intestinal epithelial receptors, together with the fact that these variants show distinguishable enzymatic activity (Genth et al., 2014; Quesada-Gómez et al., 2016; von Eichel-Streiber et al., 1995), functionally supported the notion that the TcdB subfamily is likely a cluster of toxins originated from multiple ancestral lineages (Mansfield et al., 2020; Shen et al., 2020).

The presence of TFPI in multiple cell types in the intestine, including glandular cells, endothelial cells, enterocytes, megakaryocytes, and monocytes, is consistent with the pathological observation of CDI. Colonic glands, also known as colonic crypts, are critical for the self-renew of the intestinal epithelium, producing mucus and secreting anti-microbial molecules (Clevers, 2013). Severe gut damage induced by *C. difficile* often results in erosion of crypts and loss of glandular cells (Carter et al., 2015; Smits et al., 2016). A recent study showed that TcdB2 damaged the crypt base of mouse colon in an FZDs-independent manner (Mileto et al., 2020), which could be elucidated by our findings that colonic crypts express high levels of TFPI and thus are vulnerable targets of TcdB2 and TcdB4. TcdB4 can better recognize TFPI while TcdB2 additionally binds CSPG4, which may allow them to have partially different host cell targeting preferences and further induce varied

(D) Mouse colonic tissues harvested after colon loop ligation assays were assessed for the histopathology induced by TcdB2 (2 μg) with or without CSPG4^{R1} (50 μg) or TFPI^{K2}-CSPG4^{R1} (50 μg) through H&E staining. Submucosal edema is highlighted by dashed lines. Representative images are shown. Scale bar represents 100 μm.

(E and F) Histopathological scores (n = 3 mice) for (D) were assessed based on indicated pathological features (F). Overall scores were summarized in (E).

(B, C, E, and F) Error bars indicate mean ± SEM, One-way ANOVA using Fisher LSD test for multiple comparisons. ****$p < 0.0001$, ***$p < 0.001$, **$p < 0.01$, *$p < 0.05$, ns = not significant.

pathological features. TcdB4 is a recently reported variant in clade 2 *C. difficile*; hence, clinical data for TcdB4 versus TcdB2 are limited. Future studies on the manifestations in the patients caused by TcdB4 compared to TcdB2 would be interesting.

Strikingly, over 60% of the *Tfpiβ*$^{-/-}$ mice survived in the TcdB4 challenge assay, while all the WT mice died rapidly. *Tfpiβ*$^{-/-}$mice have partial Tfpi depleted but already developed higher resistance to TcdB4, strongly supporting the idea that TFPI is a physiologically relevant receptor for clade 2 *C. difficile* TcdB in the systematic toxin exposure, which is common in severe infections. The previous toxin challenge assay showed equal lethality of TcdB1 to the WT and CSPG4 KO mice (Yuan et al., 2015), implying CSPG4 may not be critical for systematic exposure to TcdB. We further determined that the kidney is a vulnerable target under such conditions, as acute kidney damage along with rapid death was observed in the WT mice, but not *Tfpiβ*$^{-/-}$ mice. In line with our result, it was clinically reported that CDI accompanies acute kidney injury (Charilaou et al., 2018).

TFPI dampens the initiation of blood coagulation by inhibiting TF-factor VIIa complex, FXa, and prothrombinase (Maroney and Mast, 2015; Mast, 2016; Wood et al., 2013). Under the structural view, TFPI^{K2} binds to TcdB and its trypsin-like substrates (Brandstetter et al., 1996; Burgering et al., 1997) (i.e., FXa) through the same loops. Anti-TFPI therapy has recently been proposed as a novel strategy to treat coagulation disorders such as hemophilia (Chowdary, 2020; Sidonio and Zimowski, 2019). As a potent TFPI binder, TcdB4^{RBI} might be used as a new tool to study and intervene in the coagulation pathways. Besides, we postulate that the affected coagulation might bring additional advantages for *C. difficile* during the infection, whereas the exact relevance and contribution to the disease progression remains to be investigated.

Soluble TFPI and derivates are potential agents to neutralize the toxin and alleviate the intoxication caused by clade 2 *C. difficile* TcdB. Indeed, we exploited TFPI^{K2} as a potent decoy that effectively reduced tissue damage induced by TcdB4 and TcdB2 *in vivo*. Furthermore, we demonstrated that simultaneous inhibiting both TFPI and CSPG4 binding provided the best protection from TcdB2, while protection via inhibiting TFPI or CSPG4 binding alone was suboptimal. Interestingly, a similar strategy of simultaneous abolishing FZD and CSPG4 binding offered ideal protection for TcdB1 (Simeon et al., 2019). We suggest that simultaneous blocking two receptor-binding sites would be an optimal strategy for neutralizing TcdB and thus developing next-generation therapeutics for the prevention and treatment of CDI.

Limitations of the study

In this study, we defined that TcdB4 recognizes the K2 domain of TFPI for cellular entry. Because Kunitz domains are found in many varied proteins, we only tested the most closely related Kunitz domains using the GPI-fusion constructs. Despite the possibility being low, TcdB2/4 might recognize other Kunitz domain-containing proteins in full-length or untested Kunitz domains. TFPI is an important regulator for blood coagulation, and our data showed that TcdB4 could block the TFPI-FXa binding. Whether TcdB4 interferes with the coagulation pathway and contributes to the CDI pathogenesis was not investigated. It could be an interesting topic for future study. Lastly, the colon loop ligation assay was adopted to simulate the TcdB action on the colonic epithelium *in vivo*. This is a classic animal model for studying enterotoxins but only focuses on the direct impacts of toxins on host tissues. However, other factors are also involved in the CDI pathogenesis, such as bacterial colonization and immune response; whether and how TFPI-mediated TcdB2/4 intoxication plays a role in these processes remain undefined.

STAR★METHODS

Detailed methods are provided in the online version of this paper and include the following:

- KEY RESOURCES TABLE
- RESOURCE AVAILABILITY
  - Lead contact
  - Materials availability
  - Data and code availability
- EXPERIMENTAL MODEL AND SUBJECT DETAILS
  - Cell lines
  - Mice
- METHOD DETAILS
  - DNA constructs
  - Recombinant proteins
  - Cytopathic cell-rounding assay
  - Genome-wide CRISPR/Cas9 screen
  - Generating KO cell lines
  - Cell-surface binding of TcdB4
  - Immunoblot analysis
  - Cell-based toxin competition assay
  - Pull-down assays
  - Bio-layer interferometry assays
  - Cryo-EM specimen preparation and data acquisition
  - Cryo-EM data processing
  - Model building and refinement
  - Site-directed mutagenesis
  - Phylogenic analysis
  - Generating Tfpiβ KO mice
  - Colon-loop ligation assay
  - H&E staining, immunohistochemistry, and histopathological analysis
- QUANTIFICATION AND STATISTICAL ANALYSIS
  - Quantification of TcdB-induced cell rounding
  - Statistical analysis of histopathological analysis

SUPPLEMENTAL INFORMATION

Supplemental information can be found online at https://doi.org/10.1016/j.cell.2022.02.010.

ACKNOWLEDGMENTS

We thank Drs. Min Dong (Boston Children's Hospital), Hongtao Yu (Westlake University), and Dangsheng Li (Westlake University) for discussion. We also appreciate the technical support from the Biomedical Research Core Facilities

and Laboratory Animal Resources Center of Westlake University. This study was partially supported by the National Natural Science Foundation of China (grant nos. 31970129 and 31800128 to L.T. and grant no. 32171205 to Y.L.) and Zhejiang Provincial Natural Science Foundation of China (grant no. LR20C010001 to L.T. and grant no. LR20C050001 to Y.L.). L.T. and Y.L. acknowledge support from Westlake Education Foundation and Westlake Laboratory of Life Sciences and Biomedicine.

AUTHOR CONTRIBUTIONS

L.T. conceived the project. J.L., Q.Y., Y. Zhang, L.H., Y. Zhou, D.L., and L.T. carried out CRISPR screens and analysis, cell biology and biochemistry assays, and animal experiments. Q.Y., X. Zhang, L.W., X. Zhan, and Y.L. performed protein expression and purification, structure determination and analysis, and structure-based mutagenesis. J.H. and Y. Zhen helped with the bioinformatic analysis. D.J. provided key reagents and suggestions. Y.L. and L.T. designed the experiments and wrote the manuscript with input from all co-authors.

DECLARATION OF INTERESTS

Patent applications on TFPI-TcdB interactions for modulating coagulation and treating clade 2 *C. difficile* infections have been filed by Westlake University.

Received: August 13, 2021
Revised: January 11, 2022
Accepted: February 8, 2022
Published: March 17, 2022

REFERENCES

Aktories, K., Schwan, C., and Jank, T. (2017). Clostridium difficile Toxin Biology. Annu. Rev. Microbiol. *71*, 281–307.

Ascenzi, P., Bocedi, A., Bolognesi, M., Spallarossa, A., Coletta, M., De Cristofaro, R., and Menegatti, E. (2003). The bovine basic pancreatic trypsin inhibitor (Kunitz inhibitor): a milestone protein. Curr. Protein Pept. Sci. *4*, 231–251.

Badilla-Lobo, A., and Rodríguez, C. (2021). Microbiological features, epidemiology, and clinical presentation of Clostridioidesdifficile strains from MLST Clade 2: A narrative review. Anaerobe *69*, 102355.

Brandstetter, H., Kühne, A., Bode, W., Huber, R., von der Saal, W., Wirthensohn, K., and Engh, R.A. (1996). X-ray structure of active site-inhibited clotting factor Xa. Implications for drug design and substrate recognition. J. Biol. Chem. *271*, 29988–29992.

Broze, G.J., Jr., and Girard, T.J. (2012). Tissue factor pathway inhibitor: structure-function. Front. Biosci. *17*, 262–280.

Burgering, M.J., Orbons, L.P., van der Doelen, A., Mulders, J., Theunissen, H.J., Grootenhuis, P.D., Bode, W., Huber, R., and Stubbs, M.T. (1997). The second Kunitz domain of human tissue factor pathway inhibitor: cloning, structure determination and interaction with factor Xa. J. Mol. Biol. *269*, 395–407.

Carter, G.P., Chakravorty, A., Pham Nguyen, T.A., Mileto, S., Schreiber, F., Li, L., Howarth, P., Clare, S., Cunningham, B., Sambol, S.P., et al. (2015). Defining the Roles of TcdA and TcdB in Localized Gastrointestinal Disease, Systemic Organ Damage, and the Host Response during Clostridium difficile Infections. MBio *6*, e00551.

Chandrasekaran, R., and Lacy, D.B. (2017). The role of toxins in Clostridium difficile infection. FEMS Microbiol. Rev. *41*, 723–750.

Charilaou, P., Devani, K., John, F., Kanna, S., Ahlawat, S., Young, M., Khanna, S., and Reddy, C. (2018). Acute kidney injury impact on inpatient mortality in Clostridium difficile infection: A national propensity-matched study. J. Gastroenterol. Hepatol. *33*, 1227–1233.

Chaves-Olarte, E., Florin, I., Boquet, P., Popoff, M., von Eichel-Streiber, C., and Thelestam, M. (1996). UDP-glucose deficiency in a mutant cell line protects against glucosyltransferase toxins from Clostridium difficile and Clostridium sordellii. J. Biol. Chem. *271*, 6925–6932.

Chen, S., McMullan, G., Faruqi, A.R., Murshudov, G.N., Short, J.M., Scheres, S.H., and Henderson, R. (2013). High-resolution noise substitution to measure overfitting and validate resolution in 3D structure determination by single particle electron cryomicroscopy. Ultramicroscopy *135*, 24–35.

Chen, P., Tao, L., Wang, T., Zhang, J., He, A., Lam, K.H., Liu, Z., He, X., Perry, K., Dong, M., and Jin, R. (2018). Structural basis for recognition of frizzled proteins by *Clostridium difficile* toxin B. Science *360*, 664–669.

Chen, P., Lam, K.H., Liu, Z., Mindlin, F.A., Chen, B., Gutierrez, C.B., Huang, L., Zhang, Y., Hamza, T., Feng, H., et al. (2019a). Structure of the full-length Clostridium difficile toxin B. Nat. Struct. Mol. Biol. *26*, 712–719.

Chen, P., Tao, L., Liu, Z., Dong, M., and Jin, R. (2019b). Structural insight into Wnt signaling inhibition by Clostridium difficile toxin B. FEBS J. *286*, 874–881.

Chen, P., Zeng, J., Liu, Z., Thaker, H., Wang, S., Tian, S., Zhang, J., Tao, L., Gutierrez, C.B., Xing, L., et al. (2021). Structural basis for CSPG4 as a receptor for TcdB and a therapeutic target in Clostridioides difficile infection. Nat. Commun. *12*, 3748.

Chowdary, P. (2020). Anti-tissue factor pathway inhibitor (TFPI) therapy: a novel approach to the treatment of haemophilia. Int. J. Hematol. *111*, 42–50.

Chung, S.Y., Schöttelndreier, D., Tatge, H., Fühner, V., Hust, M., Beer, L.A., and Gerhard, R. (2018). The Conserved Cys-2232 in *Clostridioides difficile* Toxin B Modulates Receptor Binding. Front. Microbiol. *9*, 2314.

Clevers, H. (2013). The intestinal crypt, a prototype stem cell compartment. Cell *154*, 274–284.

Cowardin, C.A., Buonomo, E.L., Saleh, M.M., Wilson, M.G., Burgess, S.L., Kuehne, S.A., Schwan, C., Eichhoff, A.M., Koch-Nolte, F., Lyras, D., et al. (2016). The binary toxin CDT enhances Clostridium difficile virulence by suppressing protective colonic eosinophilia. Nat. Microbiol. *1*, 16108.

Donahue, B.S., Gailani, D., and Mast, A.E. (2006). Disposition of tissue factor pathway inhibitor during cardiopulmonary bypass. J. Thromb. Haemost. *4*, 1011–1016.

Emsley, P., and Cowtan, K. (2004). Coot: model-building tools for molecular graphics. Acta Crystallogr. D Biol. Crystallogr. *60*, 2126–2132.

Fletcher, J.R., Pike, C.M., Parsons, R.J., Rivera, A.J., Foley, M.H., McLaren, M.R., Montgomery, S.A., and Theriot, C.M. (2021). Clostridioides difficile exploits toxin-mediated inflammation to alter the host nutritional landscape and exclude competitors from the gut microbiota. Nat. Commun. *12*, 462.

Flores-Díaz, M., Alape-Girón, A., Persson, B., Pollesello, P., Moos, M., von Eichel-Streiber, C., Thelestam, M., and Florin, I. (1997). Cellular UDP-glucose deficiency caused by a single point mutation in the UDP-glucose pyrophosphorylase gene. J. Biol. Chem. *272*, 23784–23791.

Genth, H., Pauillac, S., Schelle, I., Bouvet, P., Bouchier, C., Varela-Chavez, C., Just, I., and Popoff, M.R. (2014). Haemorrhagic toxin and lethal toxin from Clostridium sordellii strain vpi9048: molecular characterization and comparative analysis of substrate specificity of the large clostridial glucosylating toxins. Cell. Microbiol. *16*, 1706–1721.

Girard, T.J., Tuley, E., and Broze, G.J., Jr. (2012). TFPIβ is the GPI-anchored TFPI isoform on human endothelial cells and placental microsomes. Blood *119*, 1256–1262.

Girard, T.J., Grunz, K., Lasky, N.M., Malone, J.P., and Broze, G.J., Jr. (2018). Re-evaluation of mouse tissue factor pathway inhibitor and comparison of mouse and human tissue factor pathway inhibitor physiology. J. Thromb. Haemost. *16*, 2246–2257.

Guh, A.Y., Mu, Y., Winston, L.G., Johnston, H., Olson, D., Farley, M.M., Wilson, L.E., Holzbauer, S.M., Phipps, E.C., Dumyati, G.K., et al.; Emerging Infections Program Clostridioides difficile Infection Working Group (2020). Trends in U.S. Burden of *Clostridioides difficile* Infection and Outcomes. N. Engl. J. Med. *382*, 1320–1330.

Gupta, P., Zhang, Z., Sugiman-Marangos, S.N., Tam, J., Raman, S., Julien, J.P., Kroh, H.K., Lacy, D.B., Murgolo, N., Bekkari, K., et al. (2017). Functional defects in *Clostridium difficile* TcdB toxin uptake identify CSPG4 receptor-binding determinants. J. Biol. Chem. *292*, 17290–17301.

He, M., Miyajima, F., Roberts, P., Ellison, L., Pickard, D.J., Martin, M.J., Connor, T.R., Harris, S.R., Fairley, D., Bamford, K.B., et al. (2013). Emergence

and global spread of epidemic healthcare-associated Clostridium difficile. Nat. Genet. *45*, 109–113.

Henkel, D., Tatge, H., Schöttelndreier, D., Tao, L., Dong, M., and Gerhard, R. (2020). Receptor Binding Domains of TcdB from *Clostridioides difficile* for Chondroitin Sulfate Proteoglycan-4 and Frizzled Proteins Are Functionally Independent and Additive. Toxins (Basel) *12*, E736.

Huang, Z.F., Higuchi, D., Lasky, N., and Broze, G.J., Jr. (1997). Tissue factor pathway inhibitor gene disruption produces intrauterine lethality in mice. Blood *90*, 944–951.

Hunt, J.J., and Ballard, J.D. (2013). Variations in virulence and molecular biology among emerging strains of Clostridium difficile. Microbiol. Mol. Biol. Rev. *77*, 567–581.

Huson, D.H., and Bryant, D. (2006). Application of phylogenetic networks in evolutionary studies. Mol. Biol. Evol. *23*, 254–267.

Jank, T., and Aktories, K. (2008). Structure and mode of action of clostridial glucosylating toxins: the ABCD model. Trends Microbiol. *16*, 222–229.

Knight, D.R., Imwattana, K., Kullin, B., Guerrero-Araya, E., Paredes-Sabja, D., Didelot, X., Dingle, K.E., Eyre, D.W., Rodríguez, C., and Riley, T.V. (2021). Major genetic discontinuity and novel toxigenic species in *Clostridioides difficile* taxonomy. eLife *10*, e64325.

Kuehne, S.A., Cartman, S.T., Heap, J.T., Kelly, M.L., Cockayne, A., and Minton, N.P. (2010). The role of toxin A and toxin B in Clostridium difficile infection. Nature *467*, 711–713.

Kuehne, S.A., Collery, M.M., Kelly, M.L., Cartman, S.T., Cockayne, A., and Minton, N.P. (2014). Importance of toxin A, toxin B, and CDT in virulence of an epidemic Clostridium difficile strain. J. Infect. Dis. *209*, 83–86.

Lanis, J.M., Barua, S., and Ballard, J.D. (2010). Variations in TcdB activity and the hypervirulence of emerging strains of Clostridium difficile. PLoS Pathog. *6*, e1001061.

Lee, H., Beilhartz, G.L., Kucharska, I., Raman, S., Cui, H., Lam, M.H.Y., Liang, H., Rubinstein, J.L., Schramek, D., Julien, J.P., et al. (2020). Recognition of Semaphorin Proteins by P. sordellii Lethal Toxin Reveals Principles of Receptor Specificity in Clostridial Toxins. Cell *182*, 345–356.e16.

Lei, J., and Frank, J. (2005). Automated acquisition of cryo-electron micrographs for single particle reconstruction on an FEI Tecnai electron microscope. J. Struct. Biol. *150*, 69–80.

Lessa, F.C., Mu, Y., Bamberg, W.M., Beldavs, Z.G., Dumyati, G.K., Dunn, J.R., Farley, M.M., Holzbauer, S.M., Meek, J.I., Phipps, E.C., et al. (2015). Burden of Clostridium difficile infection in the United States. N. Engl. J. Med. *372*, 825–834.

López-Ureña, D., Orozco-Aguilar, J., Chaves-Madrigal, Y., Ramírez-Mata, A., Villalobos-Jimenez, A., Ost, S., Quesada-Gómez, C., Rodríguez, C., Papatheodorou, P., and Chaves-Olarte, E. (2019). Toxin B Variants from *Clostridium difficile* Strains VPI 10463 and NAP1/027 Share Similar Substrate Profile and Cellular Intoxication Kinetics but Use Different Host Cell Entry Factors. Toxins (Basel) *11*, E348.

Lyras, D., O'Connor, J.R., Howarth, P.M., Sambol, S.P., Carter, G.P., Phumoonna, T., Poon, R., Adams, V., Vedantam, G., Johnson, S., et al. (2009). Toxin B is essential for virulence of Clostridium difficile. Nature *458*, 1176–1179.

Mansfield, M.J., Tremblay, B.J., Zeng, J., Wei, X., Hodgins, H., Worley, J., Bry, L., Dong, M., and Doxey, A.C. (2020). Phylogenomics of 8,839 Clostridioides difficile genomes reveals recombination-driven evolution and diversification of toxin A and B. PLoS Pathog. *16*, e1009181.

Maroney, S.A., and Mast, A.E. (2015). New insights into the biology of tissue factor pathway inhibitor. J. Thromb. Haemost. *13*, S200–S207.

Maroney, S.A., Ellery, P.E., and Mast, A.E. (2010). Alternatively spliced isoforms of tissue factor pathway inhibitor. Thromb. Res. *125*, S52–S56.

Mast, A.E. (2016). Tissue Factor Pathway Inhibitor: Multiple Anticoagulant Activities for a Single Protein. Arterioscler. Thromb. Vasc. Biol. *36*, 9–14.

Mileto, S.J., Jardé, T., Childress, K.O., Jensen, J.L., Rogers, A.P., Kerr, G., Hutton, M.L., Sheedlo, M.J., Bloch, S.C., Shupe, J.A., et al. (2020). *Clostridioides difficile* infection damages colonic stem cells via TcdB, impairing epithelial repair and recovery from disease. Proc. Natl. Acad. Sci. USA *117*, 8064–8073.

Ndonwi, M., Tuley, E.A., and Broze, G.J., Jr. (2010). The Kunitz-3 domain of TFPI-alpha is required for protein S-dependent enhancement of factor Xa inhibition. Blood *116*, 1344–1351.

Ndonwi, M., Girard, T.J., and Broze, G.J., Jr. (2012). The C-terminus of tissue factor pathway inhibitor α is required for its interaction with factors V and Va. J. Thromb. Haemost. *10*, 1944–1946.

Novotny, W.F., Girard, T.J., Miletich, J.P., and Broze, G.J., Jr. (1989). Purification and characterization of the lipoprotein-associated coagulation inhibitor from human plasma. J. Biol. Chem. *264*, 18832–18837.

Pan, Z., Zhang, Y., Luo, J., Li, D., Zhou, Y., He, L., Yang, Q., Dong, M., and Tao, L. (2021). Functional analyses of epidemic Clostridioides difficile toxin B variants reveal their divergence in utilizing receptors and inducing pathology. PLoS Pathog. *17*, e1009197.

Pettersen, E.F., Goddard, T.D., Huang, C.C., Couch, G.S., Greenblatt, D.M., Meng, E.C., and Ferrin, T.E. (2004). UCSF Chimera–a visualization system for exploratory research and analysis. J. Comput. Chem. *25*, 1605–1612.

Piro, O., and Broze, G.J., Jr. (2004). Role for the Kunitz-3 domain of tissue factor pathway inhibitor-alpha in cell surface binding. Circulation *110*, 3567–3572.

Piro, O., and Broze, G.J., Jr. (2005). Comparison of cell-surface TFPIalpha and beta. J. Thromb. Haemost. *3*, 2677–2683.

Pruss, K.M., and Sonnenburg, J.L. (2021). C. difficile exploits a host metabolite produced during toxin-mediated disease. Nature *593*, 261–265.

Quesada-Gómez, C., López-Ureña, D., Chumbler, N., Kroh, H.K., Castro-Peña, C., Rodríguez, C., Orozco-Aguilar, J., González-Camacho, S., Rucavado, A., Guzmán-Verri, C., et al. (2016). Analysis of TcdB Proteins within the Hypervirulent Clade 2 Reveals an Impact of RhoA Glucosylation on Clostridium difficile Proinflammatory Activities. Infect. Immun. *84*, 856–865.

Rosenthal, P.B., and Henderson, R. (2003). Optimal determination of particle orientation, absolute hand, and contrast loss in single-particle electron cryomicroscopy. J. Mol. Biol. *333*, 721–745.

Sandset, P.M., Abildgaard, U., and Larsen, M.L. (1988). Heparin induces release of extrinsic coagulation pathway inhibitor (EPI). Thromb. Res. *50*, 803–813.

Sanjana, N.E., Shalem, O., and Zhang, F. (2014). Improved vectors and genome-wide libraries for CRISPR screening. Nat. Methods *11*, 783–784.

Selzer, J., Hofmann, F., Rex, G., Wilm, M., Mann, M., Just, I., and Aktories, K. (1996). Clostridium novyi alpha-toxin-catalyzed incorporation of GlcNAc into Rho subfamily proteins. J. Biol. Chem. *271*, 25173–25177.

Shen, E., Zhu, K., Li, D., Pan, Z., Luo, Y., Bian, Q., He, L., Song, X., Zhen, Y., Jin, D., and Tao, L. (2020). Subtyping analysis reveals new variants and accelerated evolution of Clostridioides difficile toxin B. Commun. Biol. *3*, 347.

Sidonio, R.F., and Zimowski, K.L. (2019). TFPI blockade: removing coagulation's brakes. Blood *134*, 1885–1887.

Simeon, R., Jiang, M., Chamoun-Emanuelli, A.M., Yu, H., Zhang, Y., Meng, R., Peng, Z., Jakana, J., Zhang, J., Feng, H., and Chen, Z. (2019). Selection and characterization of ultrahigh potency designed ankyrin repeat protein inhibitors of C. difficile toxin B. PLoS Biol. *17*, e3000311.

Smits, W.K., Lyras, D., Lacy, D.B., Wilcox, M.H., and Kuijper, E.J. (2016). Clostridium difficile infection. Nat. Rev. Dis. Primers *2*, 16020.

Stabler, R.A., Gerding, D.N., Songer, J.G., Drudy, D., Brazier, J.S., Trinh, H.T., Witney, A.A., Hinds, J., and Wren, B.W. (2006). Comparative phylogenomics of Clostridium difficile reveals clade specificity and microevolution of hypervirulent strains. J. Bacteriol. *188*, 7297–7305.

Stabler, R.A., Dawson, L.F., Phua, L.T.H., and Wren, B.W. (2008). Comparative analysis of BI/NAP1/027 hypervirulent strains reveals novel toxin B-encoding gene (tcdB) sequences. J. Med. Microbiol. *57*, 771–775.

Stein, N. (2008). CHAINSAW: a program for mutating pdb files used as templates in molecular replacement. J. Appl. Cryst. *41*, 641–643.

Sun, X., Savidge, T., and Feng, H. (2010). The enterotoxicity of Clostridium difficile toxins. Toxins (Basel) *2*, 1848–1880.

Swint-Kruse, L., and Brown, C.S. (2005). Resmap: automated representation of macromolecular interfaces as two-dimensional networks. Bioinformatics *21*, 3327–3328.

Tao, L., Zhang, J., Meraner, P., Tovaglieri, A., Wu, X., Gerhard, R., Zhang, X., Stallcup, W.B., Miao, J., He, X., et al. (2016). Frizzled proteins are colonic epithelial receptors for C. difficile toxin B. Nature *538*, 350–355.

Tao, L., Tian, S., Zhang, J., Liu, Z., Robinson-McCarthy, L., Miyashita, S.I., Breault, D.T., Gerhard, R., Oottamasathien, S., Whelan, S.P.J., and Dong, M. (2019). Sulfated glycosaminoglycans and low-density lipoprotein receptor contribute to Clostridium difficile toxin A entry into cells. Nat. Microbiol. *4*, 1760–1769.

Terada, N., Ohno, N., Murata, S., Katoh, R., Stallcup, W.B., and Ohno, S. (2006). Immunohistochemical study of NG2 chondroitin sulfate proteoglycan expression in the small and large intestines. Histochem. Cell Biol. *126*, 483–490.

Uhlén, M., Fagerberg, L., Hallström, B.M., Lindskog, C., Oksvold, P., Mardinoglu, A., Sivertsson, Å., Kampf, C., Sjöstedt, E., Asplund, A., et al. (2015). Proteomics. Tissue-based map of the human proteome. Science *347*, 1260419.

VanInsberghe, D., Elsherbini, J.A., Varian, B., Poutahidis, T., Erdman, S., and Polz, M.F. (2020). Diarrhoeal events can trigger long-term Clostridium difficile colonization with recurrent blooms. Nat. Microbiol. *5*, 642–650.

von Eichel-Streiber, C., Meyer zu Heringdorf, D., Habermann, E., and Sartingen, S. (1995). Closing in on the toxic domain through analysis of a variant Clostridium difficile cytotoxin B. Mol. Microbiol. *17*, 313–321.

Voth, D.E., and Ballard, J.D. (2005). Clostridium difficile toxins: mechanism of action and role in disease. Clin. Microbiol. Rev. *18*, 247–263.

Wood, J.P., Bunce, M.W., Maroney, S.A., Tracy, P.B., Camire, R.M., and Mast, A.E. (2013). Tissue factor pathway inhibitor-alpha inhibits prothrombinase during the initiation of blood coagulation. Proc. Natl. Acad. Sci. USA *110*, 17838–17843.

Wood, J.P., Ellery, P.E., Maroney, S.A., and Mast, A.E. (2014). Biology of tissue factor pathway inhibitor. Blood *123*, 2934–2943.

Xu, H., Yang, J., Gao, W., Li, L., Li, P., Zhang, L., Gong, Y.N., Peng, X., Xi, J.J., Chen, S., et al. (2014). Innate immune sensing of bacterial modifications of Rho GTPases by the Pyrin inflammasome. Nature *513*, 237–241.

Yuan, P., Zhang, H., Cai, C., Zhu, S., Zhou, Y., Yang, X., He, R., Li, C., Guo, S., Li, S., et al. (2015). Chondroitin sulfate proteoglycan 4 functions as the cellular receptor for Clostridium difficile toxin B. Cell Res. *25*, 157–168.

Zhang, K. (2016). Gctf: Real-time CTF determination and correction. J. Struct. Biol. *193*, 1–12.

Zhang, J., Piro, O., Lu, L., and Broze, G.J., Jr. (2003). Glycosyl phosphatidylinositol anchorage of tissue factor pathway inhibitor. Circulation *108*, 623–627.

Zheng, S.Q., Palovcak, E., Armache, J.P., Verba, K.A., Cheng, Y., and Agard, D.A. (2017). MotionCor2: anisotropic correction of beam-induced motion for improved cryo-electron microscopy. Nat. Methods *14*, 331–332.

Zhou, Y., Li, D., Luo, J., Chen, A., Li, X., Pan, Z., Wan, L., He, L., Li, D., Li, Y., et al. (2021). Sulfated glycosaminoglycans and low-density lipoprotein receptor mediate the cellular entry of Clostridium novyi alpha-toxin. Cell Res. *31*, 935–938.

Zivanov, J., Nakane, T., Forsberg, B.O., Kimanius, D., Hagen, W.J., Lindahl, E., and Scheres, S.H. (2018). New tools for automated high-resolution cryo-EM structure determination in RELION-3. eLife *7*, e42166.

STAR★METHODS

KEY RESOURCES TABLE

REAGENT or RESOURCE	SOURCE	IDENTIFIER
Antibodies		
Rabbit polyclonal anti-TFPI	Abcam	AB180619
Chicken polyclonal anti-TcdB	List Biological Laboratories	754A
Mouse monoclonal anti-Rac1 (Clone 102)	BD Biosciences	610650; RRID: AB_397977
Mouse monoclonal anti-Rac1 (Clone 23A8)	Thermo Fisher Scientific	MA1-20580; RRID: AB_560813
Mouse monoclonal anti-HA (Clone 16B12)	BioLegend	901516; RRID: AB_2820200
Rabbit polyclonal anti-beta Actin	Abcam	AB227387
Horseradish peroxidase-labeled goat anti-rabbit IgG (H+L)	Vector Labs	PI-1000; RRID: AB_2336198
Horseradish peroxidase-labeled goat anti-mouse IgG (H+L)	Vector Labs	PI-2000; RRID: AB_2336177
Horseradish peroxidase-labeled goat anti-chicken IgY	Aves Lab	H-1004; RRID: AB_2313517
Bacterial and virus strains		
Bacillus subtilis SL401	Bacillus Genetic Stock Center	1S86
Chemicals, peptides, and recombinant proteins		
DMEM	GIBCO	C11995500
Fetal Bovine Serum	GIBCO	16000-044
Trypsin-EDTA	GIBCO	25200-072
Penicillin-Streptomycin (100X)	Sangon Biotech	H108FA0001
Puromycin	BBI	A610593-0025
Hygromycin B	Absin	Abs47014828
PolyJet	SignaGen	SL100688
Polyethylenimine Linear MW40000	Yeasen	40815ES08
Hematoxylin	Sigma	H3136
Eosin	Sigma	861006
RIPA	Beyotime	P0013B
Nitrocellulose Membrane	GE Healthcare	10600002
Protein A Agarose	Thermo Fisher Scientific	20333
Phosphoinositide Phospholipase C	Thermo Fisher Scientific	P6466
TcdB1	(Shen et al., 2020)	N/A
TcdB2	(Shen et al., 2020)	N/A
TcdB3	(Shen et al., 2020)	N/A
TcdB4	(Shen et al., 2020)	N/A
TcdB5	This paper	N/A
TcdB6	This paper	N/A
TcdB7	(Shen et al., 2020)	N/A
TcdB8	(Shen et al., 2020)	N/A
HA-TcdB4$^{1-841}$	This paper	N/A
HA-TcdB4$^{842-1834}$	This paper	N/A
HA-TcdB4$^{1801-2367}$	This paper	N/A

(*Continued on next page*)

Continued

REAGENT or RESOURCE	SOURCE	IDENTIFIER
HA-TcdB4$^{1285-1834}$	This paper	N/A
HA-TcdB4$^{1285-1834}$ L1599A	This paper	N/A
HA-TcdB4$^{1285-1834}$ K1435A	This paper	N/A
HA-TcdB4$^{1285-1834}$ L1434A	This paper	N/A
HA-TcdB4$^{1285-1834}$ L1434D	This paper	N/A
HA-TcdB4$^{1285-1834}$ V1492A	This paper	N/A
HA-TcdB4$^{1285-1834}$ L1494D	This paper	N/A
HA-TcdB4$^{1285-1834}$ M1438D	This paper	N/A
HA-TcdB4$^{1285-1834}$ D1468A	This paper	N/A
HA-TcdB4$^{1285-1834}$ P1506L	This paper	N/A
HA-TcdB4$^{1285-1834}$ F1479S	This paper	N/A
HA-TcdB4$^{1285-1834}$ E1469K	This paper	N/A
HA-TcdB4$^{1285-1834}$ I1496S	This paper	N/A
HA-TcdB4$^{1285-1834}$ Y1510C	This paper	N/A
HA-TcdB4$^{1285-1834}$ K1548E	This paper	N/A
HA-TcdB4$^{1285-1834}$ K1597N/K1600Q	This paper	N/A
HA-TcdB2$^{1285-1834}$ S1496I	This paper	N/A
Recombinant human TFPI^{K1+K2}-GFP	This paper	N/A
Recombinant human TFPIα-GFP	This paper	N/A
Recombinant human TFPI^{K1+K2}	This paper	N/A
Recombinant human TFPI^{K1+K2}-Fc	This paper	N/A
Recombinant human TFPI^{K1}-Fc	This paper	N/A
Recombinant human TFPI^{K2}-Fc	This paper	N/A
Recombinant mouse Tfpi^{K1}-Fc	This paper	N/A
Recombinant mouse Tfpi^{K2}-Fc	This paper	N/A
Human Factor Xa	Enzyme Research Laboratories	HFXa 1011
Critical commercial assays		
BCA assay	Beyotime	P0012S
2-step plus Poly-HRP Anti Rabbit/Mouse IgG Detection System (with DAB Solution)	Elabscience	E-IR-R213
DNA Gel Extraction Kit	Axygen	AP-GX-250
Midi Plasmid Kit	Axygen	AP-MX-P-25
Maxi Plasmid Kit	Axygen	AP-MX-P-10
GoldHi EndoFree Plasmid Maxi Kit	Cwbio	CW2104
PCR Clean-Up Kit	Axygen	AP-PCR-250
Blood & Cell Culture DNA Mini Kit	QIAGEN	133223
SuperSignal West Pico PLUS Lumino/ Enhancer Solution	Thermo Fisher Scientific	1863096
QuickChange II Site-Directed Mutagenesis Kit	Agilent Technologies	200523
Q5 Site-Directed Mutagenesis Kit	New England Biolabs	E0554S
Dip and Read Anti-Human IgG Fc Capture	ForteBio	18-5060
Deposited data		
CRISPR screen data	This paper	Table S1
Statistics of 3D reconstructions and model refinement	This paper	Table S2
TcdB4-TFPI map	This paper	EMD-31628
TcdB4-TFPI structure	This paper	PDB: 7VIN

(*Continued on next page*)

Continued

REAGENT or RESOURCE	SOURCE	IDENTIFIER
Experimental models: Cell lines		
Human: HeLa	ATCC	CRL-1958; RRID: CVCL_3334
Human: U2OS	ATCC	HTB-96; RRID: CVCL_0042
Human: A549	ATCC	CRM-CCL-185; RRID: CVCL_0023
Human: MCF-7	ATCC	HTB-22; RRID: CVCL_0031
Human: HT-29	ATCC	HTB-38; RRID: CVCL_0320
Human: 293T	ATCC	CRL-3216; RRID: CVCL_0063
Human: 293F	Thermo Fisher Scientific	R79007; RRID: CVCL_D603
Human: HeLa-Cas9	(Tao et al., 2016)	N/A
Human: HeLa *CSPG4*$^{-/-}$	(Tao et al., 2016)	N/A
Human: HeLa *FZD1/2/7*$^{-/-}$	(Tao et al., 2016)	N/A
Human: HeLa *CSPG4*$^{-/-}$/*FZD1/2/7*$^{-/-}$	This paper	N/A
Human: HeLa *TFPI*$^{-/-}$ (Clone F10)	This paper	N/A
Human: HeLa *TFPI*$^{-/-}$ (Clone F11)	This paper	N/A
Human: HeLa *PIGM*$^{-/-}$ (Clone B1)	This paper	N/A
Human: HeLa *PIGM*$^{-/-}$ (Clone B2)	This paper	N/A
Human: HeLa *PIGX*$^{-/-}$ (Clone D11)	This paper	N/A
Human: HeLa *PIGX*$^{-/-}$ (Clone D12)	This paper	N/A
Human: HeLa *PIGP*$^{-/-}$ (Clone G3)	This paper	N/A
Human: HeLa *PIGP*$^{-/-}$ (Clone G11)	This paper	N/A
Human: HeLa *CSPG4*$^{-/-}$/*TFPI*$^{-/-}$	This paper	N/A
Experimental models: Organisms/strains		
Mouse: C57BL/6J	Shanghai Jihui Laboratory Animal Care Co., Ltd	C57BL/6JShjh
Oligonucleotides		
oligonucleotides used in this study	This paper	Table S3
Recombinant DNA		
GeCKO v2 gRNA library	Addgene	1000000049
pMD2.G	Addgene	12259
pSPAX2	Addgene	12260
pHT01	MoBiTec	PBS001
pHT01-TcdB1-His	(Shen et al., 2020)	N/A
pHT01-TcdB2-His	(Shen et al., 2020)	N/A
pHT01-TcdB3-His	(Shen et al., 2020)	N/A
pHT01-TcdB4-His	(Shen et al., 2020)	N/A
pHT01-TcdB5-His	This paper	N/A
pHT01-TcdB6-His	This paper	N/A
pHT01-TcdB7-His	(Shen et al., 2020)	N/A
pHT01-TcdB8-His	(Shen et al., 2020)	N/A
LentiGuide-puro	Addgene	52963
LentiGuide-puro-TFPI gRNA	This paper	N/A
LentiGuide-puro-PIGM gRNA	This paper	N/A
LentiGuide-puro-PIGP gRNA	This paper	N/A
LentiGuide-puro-PIGX gRNA	This paper	N/A
PLVX-TFPIβ-IRES-Cherry	This paper	N/A
PLVX-TFPIα-IRES-Cherry	This paper	N/A
PLVX-TFPI^{K1}-GPI-IRES-Cherry	This paper	N/A
PLVX-TFPI^{K2}-GPI-IRES-Cherry	This paper	N/A

(*Continued on next page*)

Continued

REAGENT or RESOURCE	SOURCE	IDENTIFIER
PLVX-TFPI2^{K1}-GPI-IRES-Cherry	This paper	N/A
PLVX-TFPI2^{K2}-GPI-IRES-Cherry	This paper	N/A
PLVX-AMBP^{K3}-GPI-IRES-Cherry	This paper	N/A
PLVX-mouse Tfpiβ-IRES-Cherry	This paper	N/A
pCAG	Addgene	11160
pCAG-TFPI^{K1+K2}-FLAG	This paper	N/A
pCAG-TFPI^{K1+K2}-Fc-FLAG	This paper	N/A
PHLsec	Addgene	99845
pHLsec-TFPI^{K1}-Fc-His	This paper	N/A
pHLsec-TFPI^{K2}-Fc-His	This paper	N/A
pHLsec-mouse Tfpi^{K1}-Fc-His	This paper	N/A
pHLsec-mouse Tfpi^{K2}-Fc-His	This paper	N/A
pHLsec-TFPIα-eGFP-His	This paper	N/A
pHLsec-TFPI^{K1+K2}-eGFP-His	This paper	N/A
pHLsec-CSPG4^{R1} -His	This paper	N/A
pHLsec-TFPI^{K2}-CSPG4^{R1} -His	This paper	N/A
pET28a	Novagen	69864
pET28a-TcdB4$^{1-841}$-HA-His	This paper	N/A
pET28a-TcdB4$^{842-1834}$-HA-His	This paper	N/A
pET28a-TcdB4$^{1801-2367}$-HA-His	This paper	N/A
pET28a-TcdB4$^{1285-1834}$-HA-His	This paper	N/A
pET28a-TcdB4$^{1285-1834}$ L1599A-HA-His	This paper	N/A
pET28a-TcdB4$^{1285-1834}$ L1434A-HA-His	This paper	N/A
pET28a-TcdB4$^{1285-1834}$ L1434A-HA-His	This paper	N/A
pET28a-TcdB4$^{1285-1834}$ L1434D-HA-His	This paper	N/A
pET28a-TcdB4$^{1285-1834}$ V1492A-HA-His	This paper	N/A
pET28a-TcdB4$^{1285-1834}$ L1494D-HA-His	This paper	N/A
pET28a-TcdB4$^{1285-1834}$ M1438D-HA-His	This paper	N/A
pET28a-TcdB4$^{1285-1834}$ D1468A-HA-His	This paper	N/A
pET28a-TcdB4$^{1285-1834}$ P1506L-HA-His	This paper	N/A
pET28a-TcdB4$^{1285-1834}$ F1479S-HA-His	This paper	N/A
pET28a-TcdB4$^{1285-1834}$ E1469K-HA-His	This paper	N/A
pPET28a-TcdB4$^{1285-1834}$ I1496S-HA-His	This paper	N/A
pET28a-TcdB4$^{1285-1834}$ Y1510C-HA-His	This paper	N/A
pET28a-TcdB4$^{1285-1834}$ K1548E-HA-His	This paper	N/A
pET28a-TcdB4$^{1285-1834}$ K1597N/K1600Q-HA-His	This paper	N/A
pET28a-TcdB2$^{1285-1834}$-HA-His	This paper	N/A
pPET28a-TcdB2$^{1285-1834}$ S1496I-HA-His	This paper	N/A
Software and algorithms		
Octet Data Analysis Software	ForteBio	https://www.sartorius.com/en/products/protein-analysis/octet-systems-software/
GraphPad Prism v9.2.0	GraphPad Software	https://www.graphpad.com:443/
OriginPro v8.0	OriginLab	https://www.originlab.com/
SplitsTree v.4.17.0	(Huson and Bryant, 2006)	https://bibiserv.cebitec.uni-bielefeld.de/splits
AutoEMation	(Lei and Frank, 2005)	The software described will be made freely available upon request.
MotionCor2	(Zheng et al., 2017)	https://msg.ucsf.edu/em/software/motioncor2.html

(*Continued on next page*)

Continued

REAGENT or RESOURCE	SOURCE	IDENTIFIER
Gctf	(Zhang, 2016)	https://en.wikibooks.org/w/index.php?title=Software_Tools_For_Molecular_Microscopy&stable=0#Gctf
Gautomatch	developed by Kai Zhang	https://www2.mrc-lmb.cam.ac.uk/research/locally-developed-software/zhang-software/#gauto
RELION3.0	(Zivanov et al., 2018)	https://www2.mrc-lmb.cam.ac.uk/relion
CHIMERA	(Pettersen et al., 2004)	http://www.cgl.ucsf.edu/chimera
CHAINSAW	(Stein, 2008)	N/A
COOT	(Emsley and Cowtan, 2004)	https://www2.mrc-lmb.cam.ac.uk/personal/pemsley/coot/
PyMOL	Schrodinger LLC	https://www.pymol.org:443/
Other		
Fluorescence Microscope	Olympus	IX73
Inverted LSCM Confocal microscope	Olympus	FV3000
GEL Imaging System	GE Healthcare	AI680RGB
Luminescent Image Analyzer	Fuji	LAS3000
BLI System	ForteBio	Octet RED96
Histo: PEARL Tissue Processor	Leica	FC-PRL
Histo: Arcadia Paraffin Embedding Station	Leica	FC-ARC
Histo: RM2255 Microtome	Leica	FC-LRM
Histo: ST5020 Multi-stainer	Leica	FC-LST
Histo: CV5030 CoverSlipper	Leica	FC-LCV
Grid: R1.2/1.3 Au 300 mesh	Quantifoil	17080

RESOURCE AVAILABILITY

Lead contact

Further information and requests for resources and reagents should be directed to and will be fulfilled by the lead contact, Liang Tao (taoliang@westlake.edu.cn).

Materials availability

All unique/stable reagents generated in this study are available from the lead contact with a Material Transfer Agreement.

Data and code availability

The atomic coordinate for the TcdB4-TFPI complex has been deposited in the Protein Data Bank (PDB) under the accession code 7V1N. The cryo-EM map of TcdB4-TFPI has been deposited in the Electron Microscopy Data Bank (EMDB) with the accession code EMD-31628.

EXPERIMENTAL MODEL AND SUBJECT DETAILS

Cell lines

All cell lines were cultured in DMEM medium plus 10% fetal bovine serum (FBS) and 1% penicillin-streptomycin in a humidified atmosphere of 95% air and 5% CO_2 at 37°C. HeLa and 293T cells were tested negative for mycoplasma contamination and authenticated via STR profiling (Shanghai Biowing Biotechnology Co. LTD, Shanghai, China).

Mice

All the animal procedures reported herein were approved by the Institutional Animal Care and Use Committee at Westlake University (IACUC Protocol #19-010-TL). C57BL/6J mice (male and female, 6-8 weeks) were purchased from Shanghai Jihui Laboratory Animal Care Co., Ltd. (Shanghai, China). The Tfpiβ KO mice were generated in the Laboratory Animal Resources Center of Westlake University. Mice were housed with food and water without limitation and monitored under the care of full-time staff.

METHOD DETAILS

DNA constructs

Genes encoding TcdB5 (reference sequence: $TcdB_{ES130}$) and TcdB6 (reference sequence: $TcdB_{CD160}$) were codon-optimized, synthesized by Genscript (Nanjing, China), and cloned into a pHT01 vector. DNA fragments encoding $TcdB4^{1-841}$, $TcdB4^{842-1834}$, $TcdB4^{1801-2367}$, $TcdB4^{1285-1834}$, and $TcdB2^{1285-1834}$ were PCR amplified and cloned into a pET28a vector with a HA-His tag introduced to their C terminus. Genes encoding human TFPIα, TFPIβ, $TFPI^{K1}$-GPI, $TFPI^{K2}$-GPI, $TFPI2^{K1}$-GPI, $TFPI2^{K2}$-GPI, $AMBP^{K3}$-GPI, and mouse Tfpiβ were codon-optimized, synthesized by Genscript (Nanjing, China), and cloned into a PLVX-IRES-Cherry vector. DNA fragments encoding $TFPI^{K1+K2}$, $TFPI^{K1}$, $TFPI^{K2}$, $Tfpi^{K1}$, $Tfpi^{K2}$, $CSPG4^{R1}$, and $TFPI^{K2}$-$CSPG4^{R1}$ were PCR amplified and cloned into a pCAG or PHLsec vector with a FLAG, Fc-FLAG, Fc-His, or GFP-His tag fused to their C terminus.

Recombinant proteins

Recombinant full-length TcdB proteins were expressed in *Bacillus subtilis* SL401 as described previously (Shen et al., 2020). $TcdB4^{1-841}$, $TcdB4^{842-1834}$, $TcdB4^{1801-2367}$, $TcdB4^{1285-1834}$, and $TcdB2^{1285-1834}$ were expressed in *E. coli* BL21(DE3) and purified as His-tagged proteins. Recombinant TFPIα-GFP, $TFPI^{K1+K2}$-GFP, $TFPI^{K1+K2}$ $TFPI^{K1+K2}$-Fc, $TFPI^{K1}$-Fc, $TFPI^{K2}$-Fc, $Tfpi^{K1}$-Fc, $Tfpi^{K2}$-Fc, $CSPG4^{R1}$, and $TFPI^{K2}$-$CSPG4^{R1}$ were expressed in 293F cells and purified as His or FLAG-tagged proteins.

Cytopathic cell-rounding assay

The cytopathic effect (cell-rounding) of TcdB was analyzed using the gold-standard cell-rounding assay. In brief, cells were exposed to toxins for the indicated time (or 12 h, if not noted). The phase-contrast images were captured by an Olympus IX73 microscopy system (× 10-20 objectives). The numbers of round-shaped and normal-shaped cells were manually counted. The percentage of round-shaped cells was analyzed using GraphPad Prism and Origin software.

Genome-wide CRISPR/Cas9 screen

HeLa CRISPR/Cas9 genome-wide KO library was generated as previously described (Tao et al., 2019). The GeCKO v2 library is composed of two sub-libraries (A and B) targeting 19,052 human genes with six gRNAs per gene. 293T cells were used to package the lentiviruses. 48 h post-transfection, the supernatant of the 293T culture was collected. The HeLa-Cas9 cells were then transduced with the lentiviral library at a multiplicity of infection (MOI) of 0.3 and selected with 2.5 ug/mL puromycin for 4 days. For each CRISPR sub-library, at least 6.7×10^7 cells were plated onto 15-cm cell culture dishes to ensure sufficient gRNA coverage. The cell library was then added with TcdB4 of indicated concentrations and cultured for 18 h. The plates were then washed with phosphate buffer saline (PBS) to remove loosely attached cells. The remaining cells were cultured with the toxin-free medium to ~70% confluence and subjected to the next round of screen. Three rounds of screens were performed with increasing concentrations of TcdB4 (0.045, 0.15, and 0.45 pM, respectively). Cells from the final round of the screen were collected, and their genomic DNA was extracted using the Blood and Cell Culture DNA mini kit (QIAGEN). DNA fragments containing the gRNA sequences were amplified by PCR using primers lentiGP1_F and lentiGP-3_R. Next-Generation Sequencing was performed by a commercial vendor (Novogene, Beijing, China). The CRISPR screen data was provided in Table S1.

Generating KO cell lines

To generate HeLa *TFPI*$^{-/-}$, *PIGM*$^{-/-}$, *PIGP*$^{-/-}$, and *PIGX*$^{-/-}$ cells, the following gRNA sequences were cloned into the LentiGuide-Puro vector to target the indicated genes: 5′-CCTGACTCCGCAATCAACCA-3′ (*TFPI*), 5′-GTATACGGACATCGACTACC-3′ (*PIGM*), 5′-CTACAGTACTTTACCTCGTG-3′ (*PIGP*), and 5′-CGATGATAGCGGCAGTGCAC-3′ (*PIGX*). The HeLa *CSPG4*$^{-/-}$/*TFPI*$^{-/-}$ cells were generated from the HeLa *CSPG4*$^{-/-}$ cells via CRISPR/Cas9 mediated KO using the above gRNA targeting *TFPI*. Lentiviruses were produced by the co-transfection of LentiGuide-puro plasmid containing each gRNA, pSPAX2, and pMD2.G into 293T cells. HeLa-Cas9 cells were transduced with lentiviruses expressing target gRNAs. Mixed populations of infected cells were selected with puromycin (2.5 μg/mL). For all KO cells, monoclonal cells were then isolated and validated by sequencing.

Cell-surface binding of TcdB4

Cells were pre-washed with PBS and incubated with 50 nM TcdB4 on ice for 15 min. Cells were then washed three times with ice-cold PBS, scraped from the plates, lysed with RIPA, and subjected to the immunoblot analysis.

Immunoblot analysis

The protein amounts in cell lysate were determined by BCA assay (Beyotime, P0012S). The cell lysates were added with SDS sample buffer, heated for 10 min, separated on an SDS-PAGE gel, and transferred onto a nitrocellulose membrane (GE Healthcare, 10600002). The membranes were blocked with 0.5% bovine serum albumin (BSA) and 0.1% Tween-20 in tris-buffered saline at room temperature (RT) for 30 min. The membranes were then incubated with the primary antibodies overnight (4°C), washed, and incubated with secondary antibodies for 30 min. Signals were detected using the enhanced chemiluminescence substrate (Thermo Fisher Scientific, 1863096) with a Fuji LAS3000 imaging system.

Cell-based toxin competition assay

Toxins were pre-incubated with TFPI^{K1+K2}-Fc, TFPI^{K1}-Fc, or TFPI^{K2}-Fc for 10 min at room temperature with indicated toxin/protein ratios. The mixtures were added to the culture medium. Cells were then incubated at 37°C and the percentage of cell rounding was examined.

Pull-down assays

Pull-down assays were performed using Protein A agarose beads (Thermo Fisher Scientific). Briefly, Fc-tagged TFPI domains were mixed with full-length TcdB1/TcdB4 or TcdB4 fragments of indicated concentrations in 1 mL of PBS. The mixtures were incubated at 4°C for 30 min and co-precipitated by Protein A agarose beads. Beads were washed, pelleted, boiled in SDS sample buffer, and subjected to SDS-PAGE or immunoblot analysis.

Bio-layer interferometry assays

The binding affinities between recombinant TcdB4 and human/mouse TFPI domains were measured by BLI assay using the Octet RED96 system (ForteBio). All proteins were diluted in PBS. In brief, Fc-tagged human/mouse TFPI domains (10 μg/mL) were immobilized onto Dip and Read Anti-Human IgG-Fc biosensors (ForteBio) and balanced with PBS. The biosensors were then exposed to full-length TcdB4, TcdB4$^{1285-1834}$, or TcdB2$^{1285-1834}$, followed by washing (dissociation) with PBS. Binding affinities (K_d) were calculated using the Data Analysis software (ForteBio).

To analyze sequential bindings of FXa and TcdB4 to TFPI, TFPI^{K2}-Fc (10 μg /mL) was immobilized onto Dip and Read Anti-Human IgG-Fc biosensors and balanced with HNBSACa buffer (50mM HEPES, 100mM NaCl, 5mM CaCl2, 0.1% BSA, pH 7.3). The loaded biosensors were first exposed to 100 nM FXa, balanced again with HNBSACa, and then exposed to 300 nM TcdB4$^{1285-1834}$. Alternatively, the loaded biosensors were first exposed to 300 nM TcdB4$^{1285-1834}$, balanced with HNBSACa, and then exposed to 100 nM FXa. All biosensors were then washed with HNBSACa.

Cryo-EM specimen preparation and data acquisition

To prepare the cryo-EM sample, 4 μL of purified TcdB4-TFPI^{K1+K2} complex at a concentration of 9.2 mg/mL was placed on glow-discharged holey carbon grids (Quantifoil Au R2.1/3.1, 300 mesh). The grid was blotted with filter paper for 4 s in a chamber set with 100% humidity at 8°C to remove the excess sample and then plunge-frozen in liquid ethane cooled by liquid nitrogen with the Vitrobot Mark IV system (Thermo Fisher Scientific).

Cryo-EM specimens were imaged on a 300-kV Titan Krios electron microscope (Thermo Fisher Scientific) using a normal magnification of 81,000 × . Movies were recorded using a Gatan K3 detector (Thermo Fisher Scientific) equipped with a GIF Quantum energy filter (slit width 20 eV) at the counted mode, with a pixel size of 0.5435 Å. Each stack of 32 frames was exposed for 2.56 s, with a dose rate of ~23 counts/second/physical-pixel (~19.5 e-/second/Å^2) for each frame. AutoEMation II(Lei and Frank, 2005) was used for the fully automated data collection with high efficiency (~3000 stacks/24 h). All 32 frames in each stack were aligned and summed using the whole-image motion correction program MotionCor2 (Zheng et al., 2017) and binned to a pixel size of 1.087 Å. The defocus value for each image varied from −1.5 to −2.0 μm and was determined by Gctf (Zhang, 2016).

Cryo-EM data processing

A total of 4,816 micrographs were collected, of which 4,251 micrographs were manually selected for further processing (Zivanov et al., 2018). A total of 2,317,113 particles were auto-picked using Gautomatch (developed by Kai Zhang, https://www2.mrc-lmb.cam.ac.uk/research/locally-developed-software/zhang-software/#gauto) and were subjected to two-dimensional (2D) classification, resulting in 1,244,165 good particles. Then we performed two parallel runs of single-reference 3D classification using 4x binned particles (pixel size: 4.348 Å) (Round 1). After Round 1, good particles were selected and merged, and the duplicated particles were removed. The remaining 953,332 particles were applied to another two parallel runs of single-reference 3D classification (Round 2), but with 2x binned particles (pixel size: 2.174 Å). After local classification, the remaining 536,277 particles were re-centered and re-extracted (pixel size: 1.087 Å) for auto-refinement, generating a reconstruction of the TcdB4-TFPI complex at an average resolution of 4.1 Å. Then an additional round (Round 3) of 3D classification was performed. The remaining particles were classified with a soft mask on the core region of the complex. The good class containing 227,825 particles yielded a reconstruction at an average resolution of 3.1 Å. These particles were further locally classified and refined using a soft mask on the interface between TFPI and TcdB4, generating an additional reconstruction for the interface at 3.1 Å.

The angular distributions of the particles used for the final reconstruction are reasonable, and the refinement of the atomic coordinates did not suffer from severe over-fitting. The resulting EM density maps display clear features for amino acid side chains in the core region and the TcdB4-TFPI interface. Reported resolution limits were calculated based on the FSC 0.143 criterion with a high-resolution noise substitution method (Chen et al., 2013). The mask used here was generated with the following settings: lowpass filter map: 15 Å; initial binarisation threshold: 0.005; extend binary map this many pixels: 3; add a soft-edge of this many pixels: 12. Prior to visualization, all EM maps were corrected for modulation transfer function (MTF) of the detector and then sharpened by applying a negative B-factor that was estimated using an automated procedure (Rosenthal and Henderson, 2003). Local resolution variations were estimated using ResMap (Swint-Kruse and Brown, 2005).

Model building and refinement

The crystal structure of *C. difficile* toxin B (PDB code: 6OQ5) was used as a template to generate a homology model for TcdB4 using CHAINSAW (Stein, 2008). The homology model was fit into the cryo-EM map for the TcdB4-TFPI complex using UCSF Chimera (Pettersen et al., 2004). Manual adjustment of the model was performed in COOT (Emsley and Cowtan, 2004), followed by iterative rounds of real-space refinement in PHENIX and manual adjustment in COOT. Similarly, the crystal structure of the K2 domain of TFPI was fit into the cryo-EM map and manually adjusted in COOT. See Table S2 for statistics of 3D reconstructions and model refinement.

Site-directed mutagenesis

The mutations in TcdB or TcdB fragments were generated with oligonucleotides containing the mutations of interest using QuickChange II Site-Directed Mutagenesis Kit (Agilent Technologies, 200523) or Q5 Site-Directed Mutagenesis Kit (New England Biolabs, E0554S).

Phylogenic analysis

2,691 primary sequences of TcdB were directly obtained from the previous study (Shen et al., 2020). SplitsTree v.4.17.0 software (Huson and Bryant, 2006) was used to generate the phylogenic tree.

Generating Tfpiβ KO mice

The spCas9 protein and sgRNAs were microinjected into the fertilized eggs of C57BL/6 mice, sequences of sgRNAs are shown in Table S3. Fertilized eggs were transplanted to obtain positive F0 mice which were confirmed by PCR and sequencing. A stable F1 generation mouse model was obtained by mating positive F0 generation mice with C57BL/6 mice. Genotyping of mice was performed using the mouse tissue direct PCR Kit (10185ES50, Yeasen). PCR products were analyzed by agarose gel electrophoresis. Primers used for genotyping are summarized in Table S3.

Colon-loop ligation assay

All procedures were conducted following the guidelines approved by the Institutional Animal Care and Use Committee at Westlake University (IACUC Protocol #19-010-TL). 6-8 weeks old C57BL/6 female mice were anesthetized by intraperitoneal injection of 1% pentobarbital sodium. A midline laparotomy was performed to locate the ascending colon and seal a ~2 cm loop with silk ligatures. 2 μg of TcdB4 or TcdB2 with or without 100 μg of $TFPI^{K2}$-Fc, 50 μg of $CSPG4^{R1}$, or 100 μg of $TFPI^{K2}$-$CSPG4^{R1}$ in 100 μL of 0.9% normal saline or 100 μL of 0.9% normal saline were injected into the sealed colon segment using an insulin syringe, followed by suturing of the skin incision. Mice were allowed to recover in a 37°C thermostatic plate. After 6 h, mice were euthanized, and the ligated colon segments were excised. The colon segments were fixed, paraffin-embedded, sectioned, and then subjected to histopathological analysis.

H&E staining, immunohistochemistry, and histopathological analysis

Colon specimens were fixed in formalin for 12 h before being dehydrated by using an alcohol gradient, cleared with xylene then embedded in paraffin. Paraffin blocks were cut into 5 μm thick sections. The sections were stained with H&E or detected with an antibody against TFPI (ab180619, Abcam) via immunohistochemical analysis. The H&E staining sections were scored blinded by two pathologists based on edema, inflammatory cell infiltration, epithelial disruption, and cryptic damage on a scale of 0 to 3 (mild to severe). The average scores were plotted on the charts.

QUANTIFICATION AND STATISTICAL ANALYSIS

Quantification of TcdB-induced cell rounding

The phase-contrast images of cells were taken (Olympus IX73, 10-20 × objectives). A zone of 300 × 300 μm was selected randomly, which contains 50~150 cells. Round-shaped and normal-shaped cells were counted manually, and the percentage of round-shaped cells was calculated. Data were represented as mean ± SD from six independent replicates and analyzed using Student's t test in the software OriginPro or GraphPad Prism. ns, not significant; *, $p < 0.05$; **, $p < 0.01$; ***, $p < 0.001$.

Statistical analysis of histopathological analysis

The H&E staining sections were scored blinded and plotted on the charts. Data were represented as mean ± SEM and analyzed by One-way ANOVA using Fisher LSD test for multiple comparisons in the software OriginPro or GraphPad Prism. ns, not significant; *, $p < 0.05$; **, $p < 0.01$; ***, $p < 0.001$; ****, $p < 0.0001$.

Supplemental figures

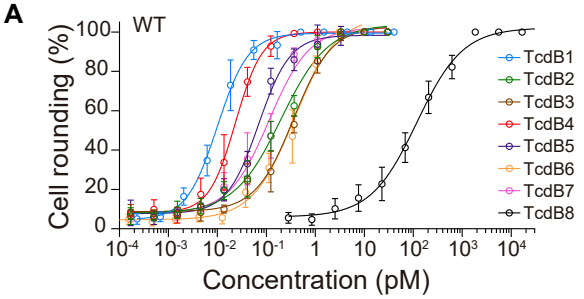

TcdB	CR_{50} (pM)
TcdB1	0.01000
TcdB2	0.2011
TcdB3	0.3587
TcdB4	0.02357
TcdB5	0.06937
TcdB6	0.3746
TcdB7	0.1138
TcdB8	118.6

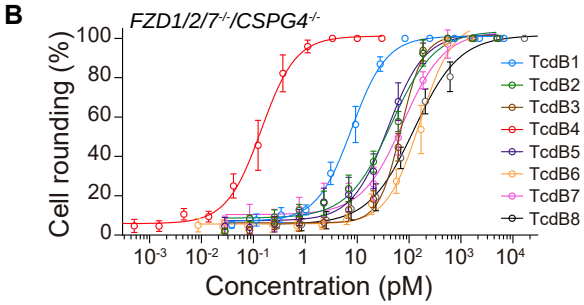

TcdB	CR_{50} (pM)
TcdB1	7.837
TcdB2	45.00
TcdB3	69.73
TcdB4	0.1415
TcdB5	39.38
TcdB6	160.4
TcdB7	75.89
TcdB8	123.6

Figure S1. TcdB4 is potent to both HeLa WT and *CSPG4*$^{-/-}$/*FZD1/2/7*$^{-/-}$ cells, related to Figure 1

(A) The sensitivities of the HeLa WT cells to eight known TcdB variants, including TcdB1, TcdB2, TcdB3, TcdB4, TcdB5, TcdB6, TcdB7, TcdB8, were measured using the cytopathic cell rounding experiments (n = 6, error bars indicate mean ± SD).

(B) The sensitivities of the HeLa *CSPG4*$^{-/-}$/*FZD1/2/7*$^{-/-}$ cells to eight known TcdB variants, including TcdB1, TcdB2, TcdB3, TcdB4, TcdB5, TcdB6, TcdB7, TcdB8, were measured using the cytopathic cell rounding experiments (n = 6, error bars indicate mean ± SD).

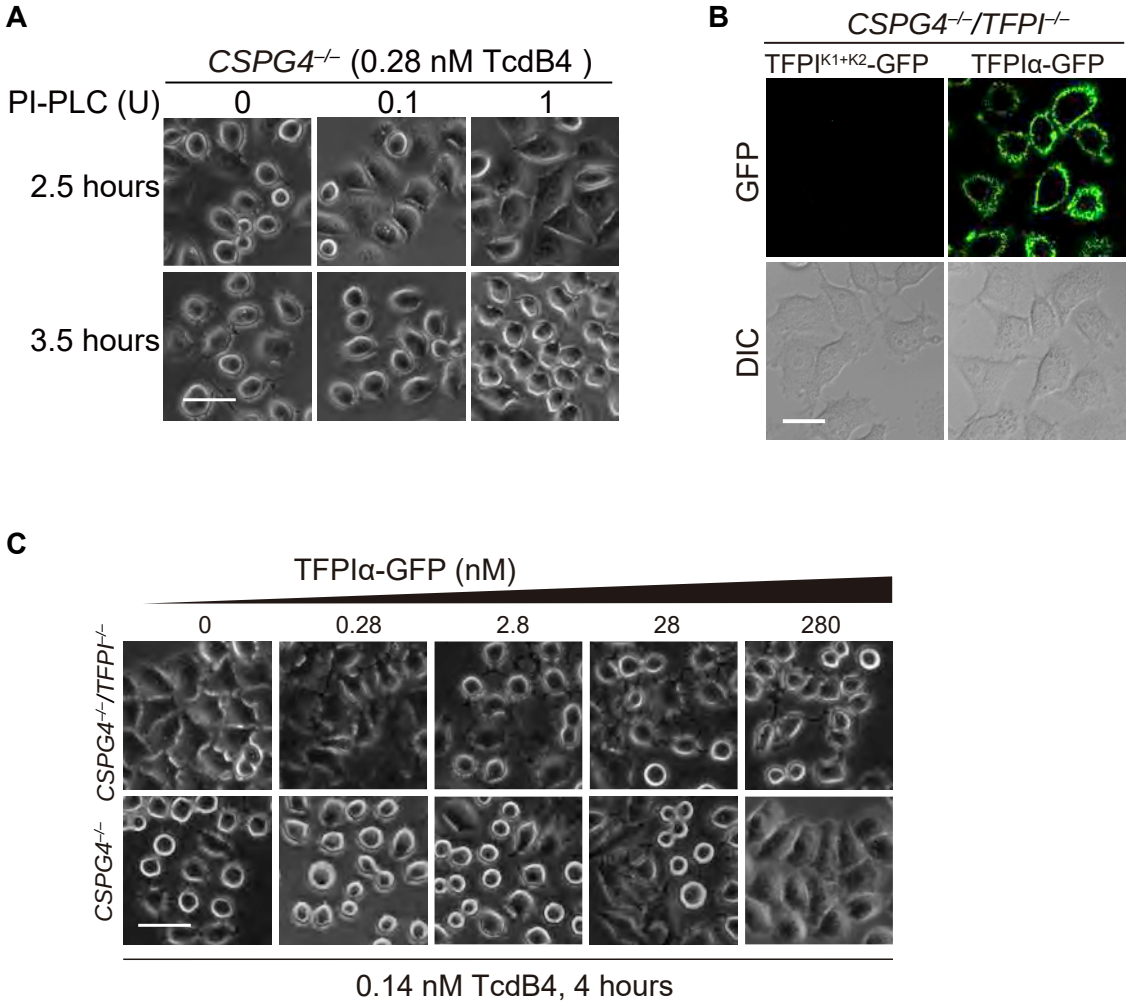

Figure S2. Membrane anchored TFPI mediates the entry of TcdB4 and soluble TFPI neutralizes TcdB4, related to Figure 2

(A) The HeLa *CSPG4*$^{-/-}$ cells were pretreated with or without PI-PLC for 30 min. Cells were then exposed to 0.28 nM TcdB4 and incubated at 37°C. Representative images of cell rounding at 2.5- and 3.5 h post-exposure to TcdB4 were shown. Scale bar represents 50 μm.

(B) Representative fluorescent images showed that supplemented TFPIα-GFP, but not TFPI^{K1+K2}-GFP, bound onto the surface of *CSPG4*$^{-/-}$/*TFPI*$^{-/-}$ cells.

(C) The HeLa *CSPG4*$^{-/-}$ and *CSPG4*$^{-/-}$/ *TFPI* $^{-/-}$ cells were exposed to 0.14 nM TcdB4 and gradient concentrations of TFPIα-GFP. Cells were then incubated at 37°C and the percentage of cell rounding was examined. Representative bright-field images of cell rounding at 4 h post-exposure to the toxin were shown. Scale bar, 50 μm.

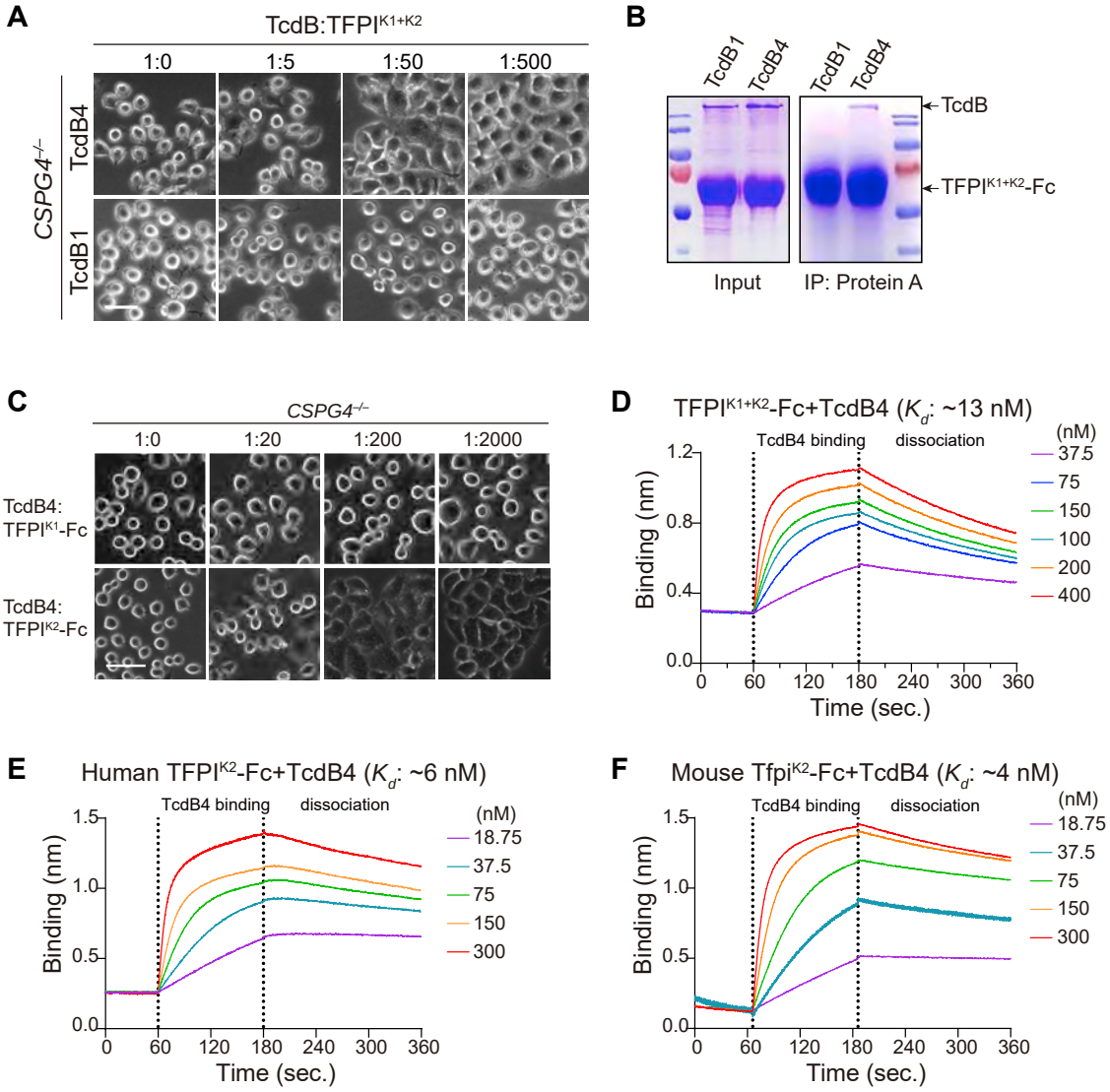

Figure S3. TcdB4 specifically binds to TFPI, related to Figure 3

(A) TFPI^{K1+K2}-Fc protects the HeLa *CSPG4*$^{-/-}$ cells from TcdB4 but not TcdB1 as measured by the cell rounding assay.

(B) The pull-down assay showed that TcdB4, but not TcdB1, binds to Fc-tagged TFPI^{K1+K2}.

(C) Purified TFPI^{K2}-Fc, but not TFPI^{K2}-Fc, protects *CSPG4*$^{-/-}$ cells from TcdB4 as measured by the cell rounding assay. Scale bar represents 50 μm.

(D) Representative binding curves of TcdB4 to Fc-tagged human TFPI^{K1+K2} were examined by BLI assays.

(E) Representative binding curves of TcdB4 to Fc-tagged human TFPI^{K2}.

(F) Representative binding curves of TcdB4 to Fc-tagged mouse Tfpi^{K2}.

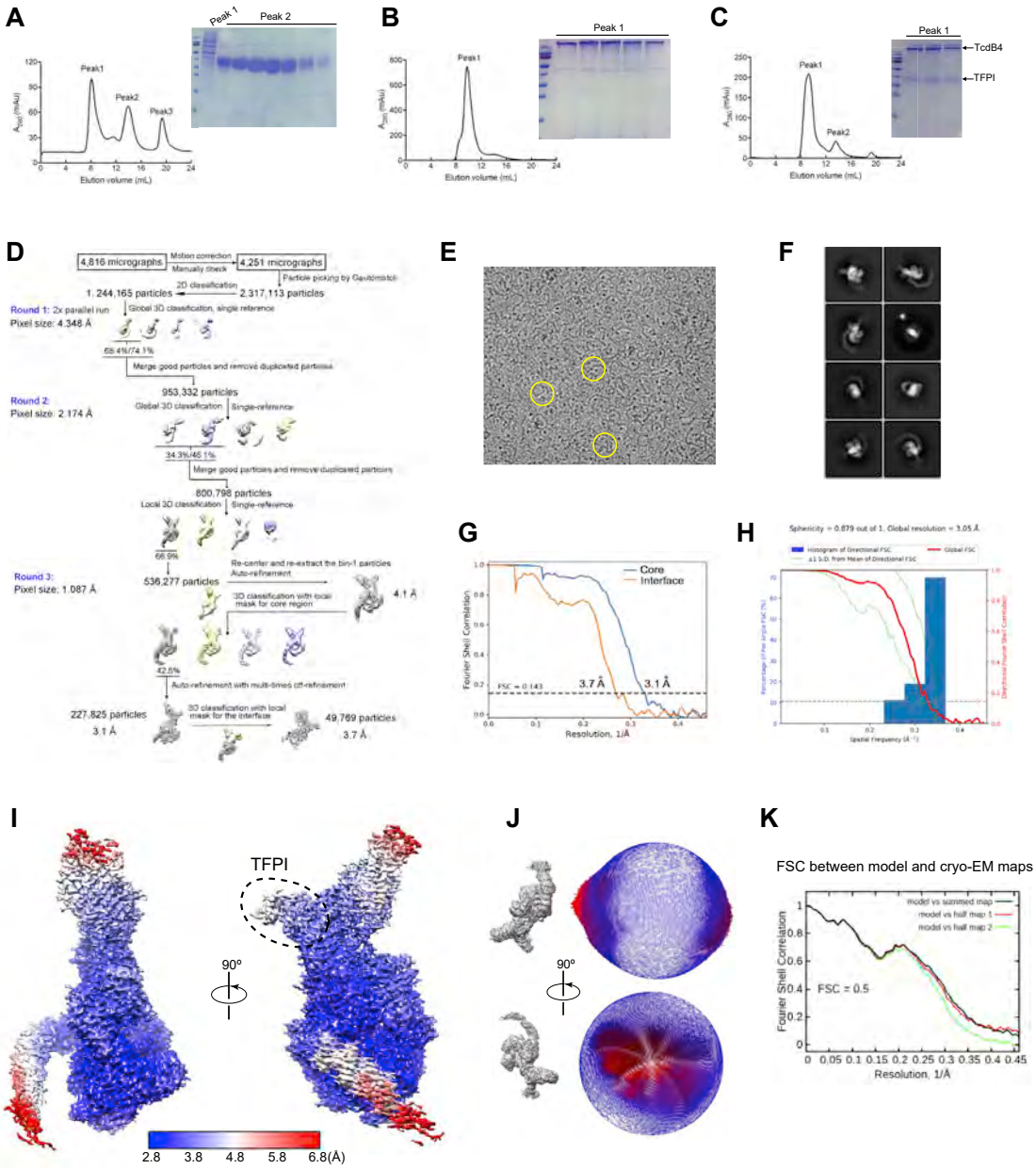

Figure S4. Purification of TcdB4-TFPI complex and single-particle cryo-EM image processing and analysis, related to Figure 4

(A) Size exclusion chromatography profile of TFPI and SDS-PAGE of the peak fraction shown in the inset.

(B) Size exclusion chromatography profile of TcdB4 and SDS-PAGE of the peak fraction shown in the inset.

(C) Size exclusion chromatography profile of TcdB4-TFPI complex and SDS-PAGE of the peak fraction shown in the inset.

(D) Flow chart for cryo-EM data processing. For details, see "cryo-EM data processing" in the STAR Methods section.

(E) Representative cryo-EM image of TcdB4-TFPI. Some single-particles for TcdB4-TFPI are highlighted by cyan circles.

(F) Two-dimensional class averages of cryo-EM particle images of TcdB4-TFPI.

(G) The final reconstruction for the TcdB4-TFPI complex displays an average resolution of 3.1 Å based on the FSC value of 0.143.

(H) Histogram and directional FSC plot for the EM map of TcdB4-TFPI complex.

(I) Local resolution of the final cryo-EM map of the TcdB4-TFPI complex.

(J) Angular distribution of particle images included in the final 3D reconstruction.

(K) FSC curve of TcdB4-TFPI between the atomic model and the final map with indicated resolution at FSC = 0.5 (black); FSC curve between half map 1 (red) or half map 2 (green) and the atomic model refined against half map 1.

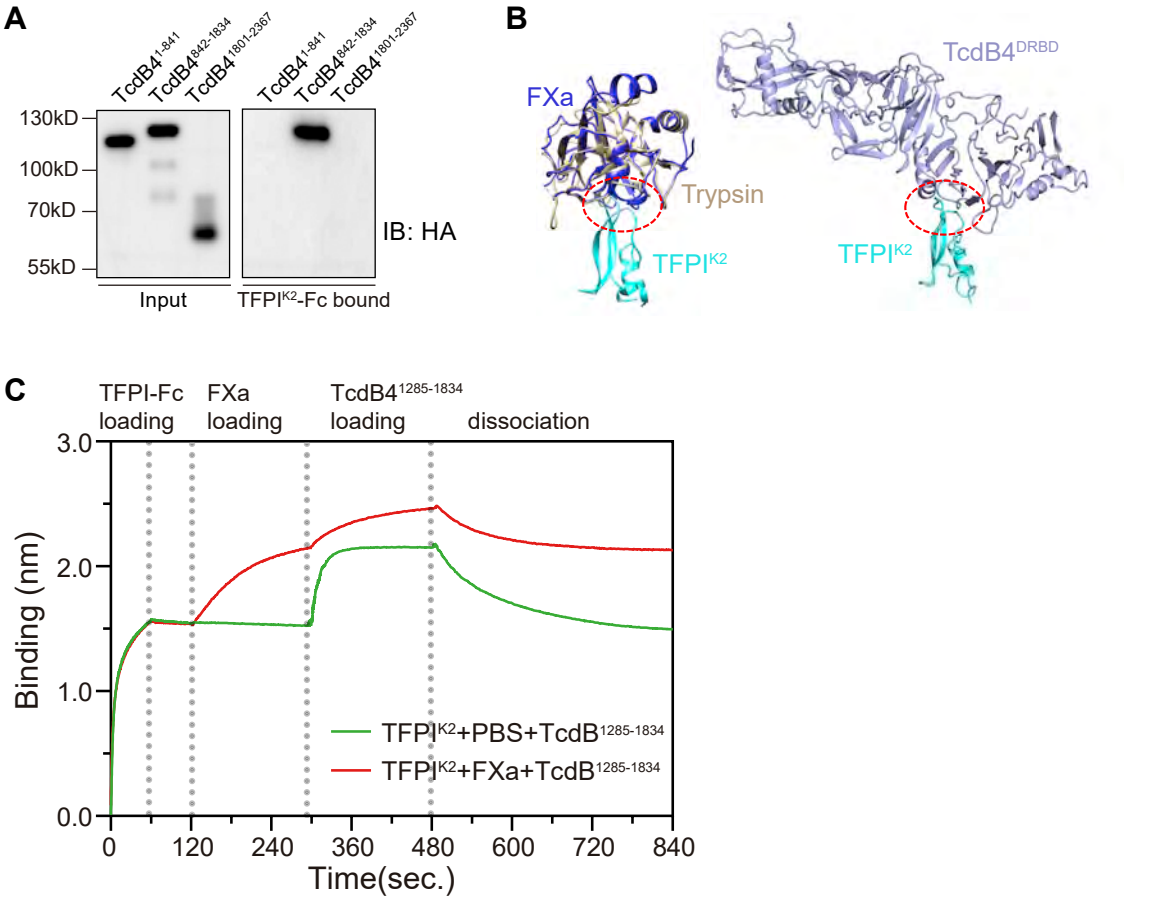

Figure S5. TcdB4 and FXa competitively bind to TFPI, related to Figure 4

(A) Fc-tagged TFPI^{K2} binds to TcdB4$^{842-1834}$, but not to TcdB4$^{1-841}$ and TcdB4$^{1801-2367}$ shown by the immunoblot analysis.

(B) Comparison between the structures of TFPI-FXa/Trypsin (PDB: 1TFX and 1FAX, left panel) and TFPI-TcdB4 complex (right panel). Their interfaces are marked by red circles.

(C) Preloading FXa to TFPI^{K2} impeded subsequent binding of TcdB4$^{1285-1834}$. The TFPI^{K2}-Fc loaded biosensors were first exposed to 100 nM FXa or control buffer, balanced, and then exposed to 300 nM TcdB4$^{1285-1834}$.

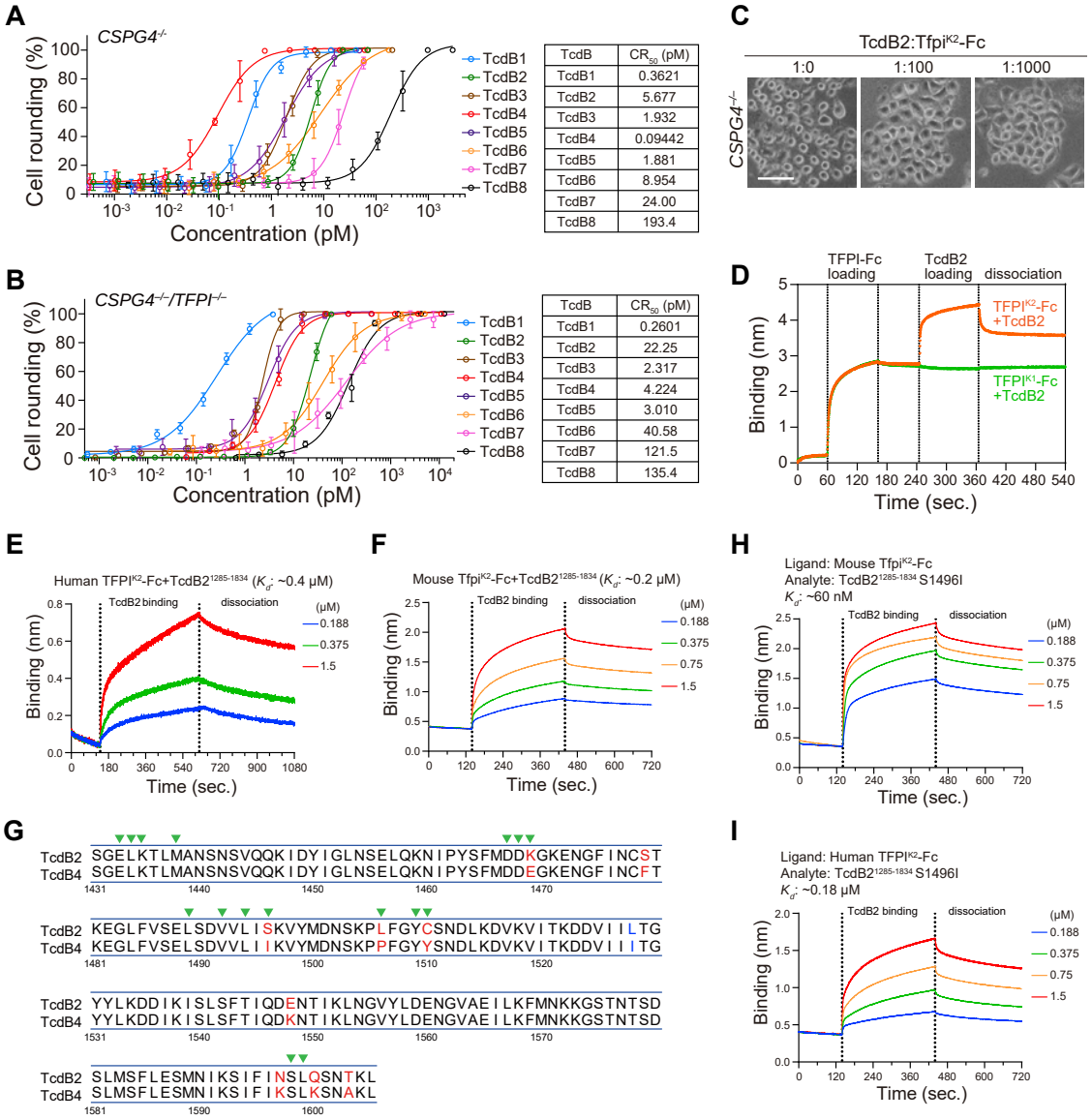

TcdB	CR_{50} (pM)
TcdB1	0.3621
TcdB2	5.677
TcdB3	1.932
TcdB4	0.09442
TcdB5	1.881
TcdB6	8.954
TcdB7	24.00
TcdB8	193.4

TcdB	CR_{50} (pM)
TcdB1	0.2601
TcdB2	22.25
TcdB3	2.317
TcdB4	4.224
TcdB5	3.010
TcdB6	40.58
TcdB7	121.5
TcdB8	135.4

Figure S6. TFPI interacts with TcdB2, related to Figure 5

(A) The sensitivities of the HeLa *CSPG4*$^{-/-}$ cells to TcdB1-8 were measured using the cytopathic cell rounding experiments (n = 6, error bars indicate mean ± SD).

(B) The sensitivities of the HeLa *CSPG4*$^{-/-}$/ *TFPI*$^{-/-}$ cells to TcdB1-8 were measured using the cytopathic cell rounding experiments (n = 6, error bars indicate mean ± SD).

(C) The HeLa *CSPG4*$^{-/-}$ cells were exposed to 100 pM TcdB2 with or without Fc-tagged mouse Tfpi^{K2}. Cells were then incubated at 37°C and the percentage of cell rounding was examined. Representative bright-field images of cell rounding at 4 h post-exposure to the toxin were shown. Scale bar represents 100 μm.

(D) Characterization of TcdB2 binding to Fc-tagged TFPI^{K1} or TFPI^{K2} using the BLI assay.

(E) Representative binding curves of TcdB2$^{1285-1834}$ to Fc-tagged human TFPI^{K2}.

(F) Representative binding curves of TcdB2$^{1285-1834}$ to Fc-tagged mouse Tfpi^{K2}.

(G) Sequence alignment between the RBIs of TcdB2 and TcdB4. Non-conserved residues are marked in red, similar residues are marked in blue. Residues that contribute to the TFPI binding are denoted by green triangles.

(H) Representative binding curves of TcdB2$^{1285-1834}$ S1496I mutant to Fc-tagged mouse Tfpi.

(I) Representative binding curves of TcdB2$^{1285-1834}$ S1496I mutant to Fc-tagged human TFPI.

CellPress

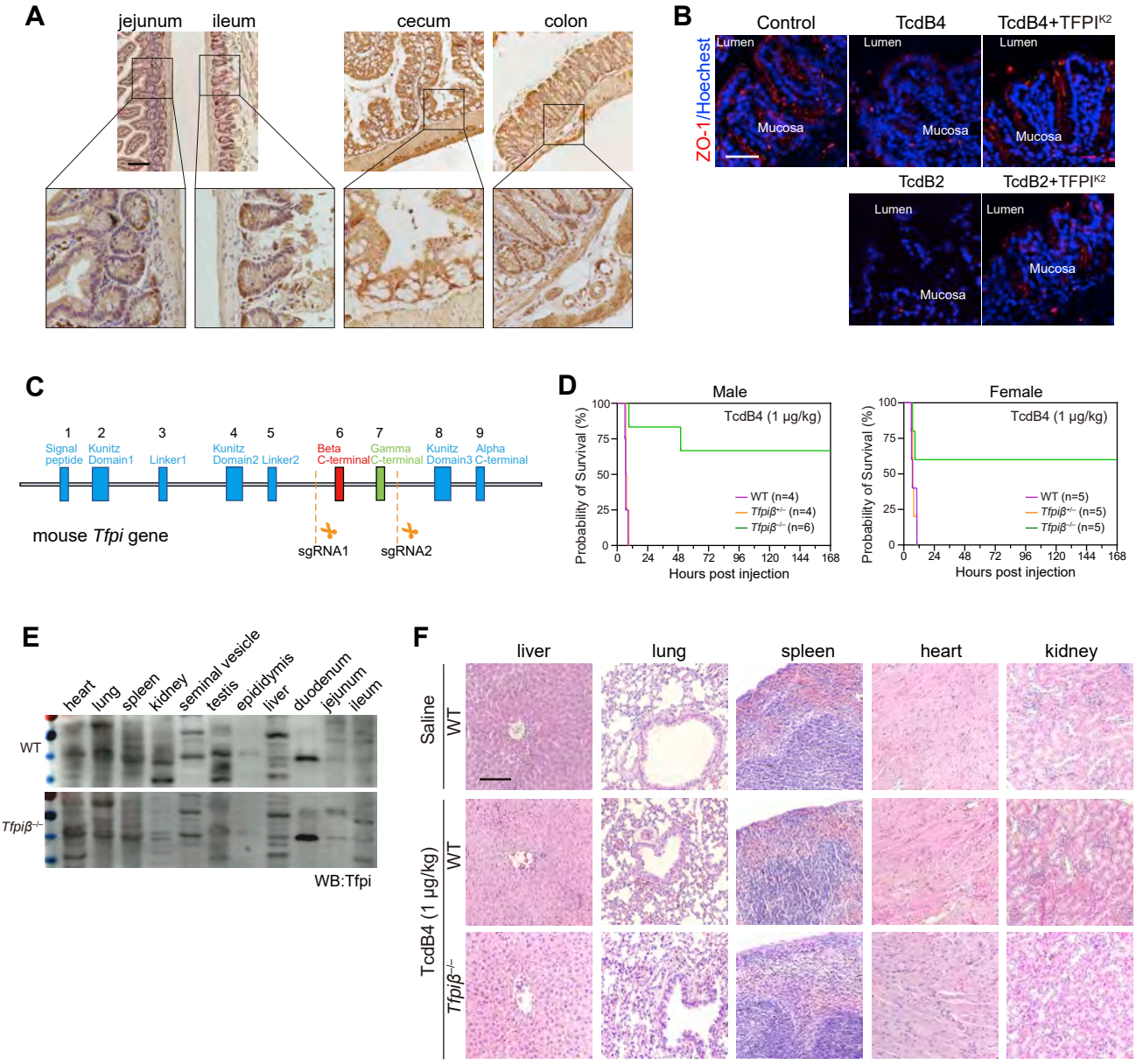

Figure S7. TFPI is a physiologically relevant receptor for clade 2 *C. difficile* TcdB, related to Figure 6

(A) Low-magnification images of immunochemical staining show overviews of mouse Tfpi distribution in ileum, jejunum, cecum, and colon. The zoomed regions shown in Figure 6A are boxed. Scale bar represents 100 μm.

(B) Immunofluorescent staining of epithelial cell tight junction marker ZO-1 (red) in mouse colonic tissues harvested after colon-loop ligation assays. Cell nuclei were stained by Hoechst (blue). Scale bar represents 100 μm.

(C) Schematic diagram of the experimental design of knocking out the *Tfpiβ* isoform from the mouse genome using the CRISPR-Cas9 approach.

(D) The Kaplan-Meier survival curves of the WT, *Tfpiβ*$^{+/-}$, *Tfpiβ*$^{-/-}$ mice after i.p. injection of 1 μg/kg TcdB4 (monitored for seven days), separated by the genders.

(E) The immunoblot analysis of Tfpi expression in various organs from the WT and *Tfpiβ*$^{-/-}$ mice.

(F) The histological analysis shows that i.p. injection of 1 μg/kg TcdB4 leads to acute kidney damage in the WT mice, but not the *Tfpiβ*$^{-/-}$ mice. Livers, lungs, spleens, and hearts from all mice seem to be normal. Scale bar represents 100 μm.